Coastal Engineering 185 (2023) 104362

Contents lists available at ScienceDirect

Coastal Engineering

journal homepage: www.elsevier.com/locate/coastaleng

Large-scale wave breaking over a barred beach: SPH numerical simulation and comparison with experiments

Corrado Altomare [a], Pietro Scandura [b,*], Iván Cáceres [a], Dominic A. van der A [c], Giacomo Viccione [d]

[a] Laboratori d'Enginyeria Marítima, Universitat Politècnica de Catalunya, 6, 08034, Barcelona, Spain
[b] Department of Civil Engineering and Architecture, University of Catania, Via Santa Sofia, 64, Catania, 95123, Italy
[c] School of Engineering, University of Aberdeen, King's College, Aberdeen, AB24 3UE, Scotland
[d] Department of Civil Engineering, University of Salerno, via Giovanni Paolo II 132, Fisciano, SA, 84084, Italy

ARTICLE INFO

Keywords:
Wave breaking
Barred beach
Smoothed particle hydrodynamics
DualSPHysics solver
Numerical validation

ABSTRACT

Wave breaking plays a crucial role in several areas of interest in coastal engineering, such as flooding, wave loading on structures and coastal morphodynamics. In the present study, Smoothed Particle Hydrodynamics (SPH) simulations of monochromatic waves breaking over a rigid barred beach profile are presented. The numerical results comprise wave heights, phase average velocities, time-averaged velocities, vorticity dynamics, and radiation stress, and are validated versus detailed water surface and velocity measurements carried out in a large-scale laboratory wave flume. The experimental data include velocity profiles below the wave trough measured at 22 cross-shore locations in the bar region using acoustic and optical techniques and water surface elevation measured along the flume using resistive gauges, acoustic gauges and pressure sensors.

This study is novel in that it analyses the hydrodynamics of wave breaking at a scale close to natural conditions, thus significantly reducing the scale effects of most previous studies, which were conducted at a much smaller scale.

In general, water surface elevation is well reproduced by SPH, but discrepancies with the experiments are observed in the highly aerated breaking region, depending on the measurement technique.

The SPH simulation shows that wave breaking generates a recirculating cell, immediately above the trough of the bar. Within this cell, near the bed, the flow is offshore directed, while in the upper part of the water column it is onshore oriented. This flow is probably one of the mechanisms that determine the growth of the bar when the bed is made of mobile material. The time-averaged velocity profiles are reproduced with reasonable accuracy by the numerical model, except at the edges of the bar trough, where discrepancies with respect to the measurements are observed. The numerical results provide detailed information, particularly interesting in areas lacking experimental data. One of the main surprising features revealed by the SPH simulations is the generation of a vortex pair that occurs when the cavities formed by the plunge jet collapse. These vortices can occasionally deform the free surface.

Based on the numerical results, an analysis of the terms contributing to radiation stress shows that the product between the horizontal and the vertical velocity components does not make a significant contribution. Through comparisons with the SPH results, it is observed that the linear wave theory provides correct estimates of the radiation stress in the shoaling region sufficiently far from the bar crest, while in the surf zone it reproduces incorrect results.

Information about the appropriate SPH model setup to correctly capture the physical processes involved in the breaking phenomenon are also presented.

1. Introduction

Wave-breaking induced hydrodynamics has been the subject of several studies over the last few decades (Lowe et al., 2022, 2019; Wei et al., 2018; Lupieri and Contento, 2015; Torres-Freyermuth et al., 2007), due to the importance of wave breaking on e.g., beach morphodynamics (Rafati et al., 2021; Anthony and Aagaard, 2020; van Thiel de

* Corresponding author.
E-mail address: pietro.scandura@unict.it (P. Scandura).

https://doi.org/10.1016/j.coastaleng.2023.104362
Received 21 February 2023; Received in revised form 30 June 2023; Accepted 12 July 2023
Available online 19 July 2023

Vries et al., 2008), wave loading on structures (Wienke and Oumeraci, 2005) and the interaction of waves with coastal ecosystems (Lee et al., 2021). Coastal areas are particularly vulnerable to meteorological factors and to the climate change effects (Hughes et al., 2018), such as sea level rise and increasing frequency of storms (Viccione and Izzo, 2022; Kelebek et al., 2021; Pelosi et al., 2020), therefore the availability of reliable hydro-morphodynamic numerical models, able to predict the impact of waves on the coastal areas remains of crucial importance. The surf zone is an area that is still subject to important shortcomings in terms of understanding, particularly for sandy barred beaches (Dubarbier et al., 2017; Ruessink et al., 2016). Nearshore bars are common features of sandy beaches, both for swell-dominated and storm-dominated wave environments, yet most previous experimental and numerical studies on wave breaking focused on plane sloping beaches.

Over the past decades, several numerical models have been developed to describe wave breaking phenomena. In general, these models are developed by introducing appropriate simplifications to the continuity and momentum equations. Depending on the extent of these simplifications, a model can potentially reproduce all or some of the hydrodynamic processes in the breaking and surf zones. For example, Elsayed et al. (2022) reported that adjusting the energy dissipation parameter of a single-layer or two-layer non-hydrostatic mathematical model, could improve the prediction of wave height, but not the flow velocity.

Existing numerical models to describe wave breaking encompass a wide range of approaches, such as irrotational wave theory (Grilli et al., 2001), Boussinesq approximation (Tissier et al., 2012), Reynolds Averaged Navier Stokes equations (Jacobsen et al., 2014) and Large Eddy Simulation (Zhou et al., 2017). The models mentioned above are based on the Eulerian approach, therefore, the system of differential equations of each model is solved on a fixed grid by means of finite difference or finite volume methods. However, models based on this approach can be impractical in reproducing the highly deformed interfaces occurring during wave breaking. In these cases, Lagrangian approaches provide a more straightforward way to calculate the position of the free surface and solve the continuity and momentum equations. The meshless and Lagrangian Smoothed Particle Hydrodynamics (SPH) method, originally developed in astrophysics (Lucy, 1977), has proved to be well suited to simulate highly nonlinear flows with interfaces undergoing large deformation (e.g. Dalrymple and Rogers, 2006; Khayyer et al., 2018; Crespo et al., 2017).

The SPH method has been used to study a variety of problems in coastal hydrodynamics, such as wave run-up (Zhang et al., 2018; Altomare et al., 2014), and loading on structures (Altomare et al., 2015; González-Cao et al., 2019; Altomare et al., 2020) and wave overtopping (Shao et al., 2006; Altomare et al., 2021; Suzuki et al., 2022).

SPH has also been used to investigate wave breaking hydrodynamics in the surf zone. Farahani et al. (2013) modelled the mean wave-induced nearshore circulation created by breaking waves in a simplified bar/rip channel. Wei et al. (2017) investigated short-crested wave breaking over a planar beach and the associated wave-current interactions and vortex generation. Makris et al. (2016) investigated near-shore wave breaking over a relatively mild slope and highlighted the importance of model resolution to resolve the two-dimensional kinematics and dynamics at turbulent flow scales. De Padova et al. (2018) analysed the vorticity generation by plunging wave breaking both in the pre-breaking and breaking zone. Recently, Tazaki et al. (2022) studied the sediment transport mechanisms under plunging breaking waves using the moving particle semi-implicit (MPS) method coupled with the discrete element method (DEM). They found that the near-bed sediment motion was mainly determined by the pressure gradient due to eddies generated by the plunging waves.

Zago et al. (2021) focused on the excessive energy dissipation of sea wave when using the standard SPH formulation and following Oger et al. (2007) developed an approach based on the kernel gradient correction that ensures reciprocity during particle interaction and conserves momentum and energy.

The list of existing SPH literature on nearshore breaking and surf-zone hydrodynamics is not fully exhaustive here, however all existing studies have in common that they considered simple planar beach profiles. The assessment of relevant surf zone hydrodynamic processes using SPH for a barred beach profile has not been reported. In addition, most of the studies on this topic have considered small waves, where the ratio of inertial to viscous forces is much smaller than in natural waves, so large scale effects are involved. The novelty of this study is twofold: (1) it analyses the hydrodynamics generated by breaking waves at a scale close to natural field conditions, thus reducing the scale effects present in small-scale experiments; (2) it analyses wave breaking on a barred beach profile, which is a more realistic situation compared to the constant sloping beach profiles considered in most previous studies. The general objective of the study is to improve the understanding of the physical processes generated by breaking waves and to determine the SPH model setup that provides the best compromise between accuracy and computational effort.

In the present paper, the DualSPHysics solver (Domínguez et al., 2022), based on the Smoothed Particle Hydrodynamics method, is used to model wave breaking on a barred beach, including the shoaling and the surf zones.

The simulations are compared against new laboratory data obtained in the CIEM large-scale wave flume under monochromatic plunging breaking wave over a fixed barred beach profile. The measurements were part of a broader experimental program, including the investigation of wave breaking hydrodynamics under bichromatic wave conditions (van der Zanden et al., 2019). In this paper we focus on the previously unpublished measurements involving a monochromatic wave condition. These experiments involve an unprecedented number of cross-shore measurements positions, compared to previous measurements carried out in the same flume (van der A et al., 2017). In this study, the new experimental results are used to validate the SPH model results, but also to provide additional insights into the hydrodynamic processes occurring under breaking waves.

2. Smoothed particle hydrodynamics method and SPH solver

In SPH the fluid continuum is discretized in a finite number of particles, which represent calculation nodal points free to move in space in a full Lagrangian framework. All particle properties (e.g. position, velocity, acceleration, density, pressure) are calculated at each numerical time step by interpolating the values of a set of neighbouring particles. The area of influence that determines the interaction between the ith particle and its neighbours is defined using a characteristic radius or smoothing length (h_{SPH}), where the weighting of the contribution of each particle depends on the weighted kernel function (W). A Quintic kernel (Wendland, 1995) is employed in the present study, where no particle interaction is considered for initial particle spacing greater than $2 \times h_{SPH}$. Employing a discrete SPH formalism, based on integral interpolants and the properties of the weighting function (Monaghan, 1992), the continuity and momentum equations can be written as follows:

$$\frac{d\varrho_a}{dt} = \sum_b m_b \left(\mathbf{u}_a - \mathbf{u}_b\right) \cdot \nabla_a W_{ab} + D, \tag{1}$$

$$\frac{d\mathbf{u}_a}{dt} = -\sum_b \left(\frac{P_b + P_a}{\varrho_b \varrho_a} + \Pi_{ab} \right) \nabla_a W_{ab} + \mathbf{g}, \tag{2}$$

where t is the time, ϱ_a and ϱ_b are the densities of particles a and b respectively, m_b is the mass of particle b, $\mathbf{u}_a = d\mathbf{r}_a/dt$ and $\mathbf{u}_b = d\mathbf{r}_b/dt$ with $\mathbf{r}_k$ and $\mathbf{u}_k$ being the particle position and velocity respectively, P_k is the pressure, $\mathbf{g}$ is the gravitational acceleration, W_{ab} is the kernel function that depends on the ratio between the distance between

particles a and b and the smoothing length. In Eq. (1) D is the density diffusion term proposed by Fourtakas et al. (2019), given by Eq. (3),

$$D = 2\,\delta\,h_{SPH}\,\overline{c_{ab}}\sum_b\left(\varrho_b-\varrho_a\right)\frac{\mathbf{r}_{ab}\cdot\nabla_a W_{ab}}{r_{ab}^2}\frac{m_b}{\varrho_b}, \tag{3}$$

where $\mathbf{r}_{ab}=\mathbf{r}_a-\mathbf{r}_b$, $\overline{c_{ab}}=0.5(c_a+c_b)$ is the mean speed of sound and $\delta=0.1$. In the momentum equation Π_{ab} is the artificial viscosity term proposed by Monaghan (1992):

$$\Pi_{ab}=\begin{cases}\dfrac{-\alpha\,\overline{c_{ab}}\,\mu_{ab}}{\overline{\varrho_{ab}}} & \text{if}\quad \mathbf{u}_{ab}\cdot\mathbf{r}_{ab}<0,\\ 0 & \text{if}\quad \mathbf{u}_{ab}\cdot\mathbf{r}_{ab}\geq 0,\end{cases} \tag{4}$$

where $\mathbf{u}_{ab}=\mathbf{u}_a-\mathbf{u}_b$, $\mu_{ab}=h_{SPH}\mathbf{u}_{ab}\cdot\mathbf{r}_{ab}/(r_{ab}^2+\eta^2)$, $\eta^2=0.001\times h_{SPH}^2$ is a parameter to prevent singularities and α is a coefficient that needs to be tuned. Altomare et al. (2015) proposed a reference value of $\alpha=0.01$ that is based on model validation against experimental data for wave propagation and induced loading onto coastal structures.

The linear term in the velocity difference expressed in Eq. (4) is linked to the real shear and bulk viscosity of the continuum (Monaghan, 1985). Higher order terms introduced to handle high Mach number shocks are neglected for applications of free surface flows. The artificial viscosity generates a repulsive force when two particles approach each other, otherwise it vanishes.

Gotoh et al. (2001) presented pioneering work in which the sub-particle Reynolds stress terms were estimated using the Smagorinsky eddy viscosity model through an LES-type scheme referred to as the SPS (Sub-Particle-Scale) turbulence model for the particle methods. Their method showed good agreement with experiments when reproducing the dynamics of a turbulent free jet. In Dalrymple and Rogers (2006) further analysis of the importance of LES-based sub-particle scale (SPS) approaches to model coherent turbulent flow structure in breaking waves is provided. Very recently, Lowe et al. (2022) employed Laminar+SPS scheme in DualSPHysics to study reef surf zone processes driven by plunging irregular waves: an improvement in the model accuracy was found compared to using an artificial viscosity, with slightly less dissipation occurring right after the start of wave breaking. Nevertheless, Lowe et al. (2022) remark that the LES-type scheme "would only describe the 2D features of surf zone eddies and thus cannot resolve the small-scale 3D turbulent flow structures that are required to properly resolve the turbulent energy cascade from large- to small-scale eddies where turbulent kinetic energy is dissipated". This fact has already been pointed out by Altomare et al. (2021) and Meringolo et al. (2018). Given the conceptual implications of using SPS in a 2D modelling, in this study we preferred to use the artificial viscosity and investigate its effect on the accuracy of the numerical model.

Gotoh and Khayyer (2018) presented a comprehensive review of the state-of-art of particles methods for ocean and coastal engineering, where Weakly Compressible and Incompressible SPH methods, respectively WCSPH and ISPH, are described and compared. WCSPH and ISPH differ mainly in the way they solve the pressure and density fields. In a WCSPH solver, such as DualSPHsysics (Domínguez et al., 2022) used in the present work, an appropriate equation of state is solved in a fully-explicit manner. Following Monaghan (1994), pressure and density are related by Tait's equation of state as follows:

$$P=B\left[\left(\frac{\varrho}{\varrho_0}\right)^{\gamma}-1\right], \tag{5}$$

where $\gamma=7$ is the polytropic constant and $B=c_0^2\varrho_0/\gamma$ depends on the reference density ϱ_0 and on the speed of sound c_0. The equation of state is stiff: oscillations in the density field are allowed within a range of 1%. Usually this is achieved by maintaining the speed of sound at least 10 times higher than the maximum velocity in the system by adjusting the compressibility of the fluid.

DualSPHysics is written in two languages, namely C++ and CUDA, and optimized to use the parallel processing power of either CPUs and/or GPUs (Domínguez et al., 2013). GPUs offer greater computing power than CPUs, and they are an affordable option to accelerate SPH modelling, making the study of real engineering-scale problems possible (Altomare et al., 2014; Domínguez et al., 2019). Within SPH, a single (optimum) approach to incorporate solid boundaries in fluid mechanics applications has yet to be established, with improvement of boundary conditions being specified by the SPH community as a priority research topic (Vacondio et al., 2021). In DualSPHysics, the interaction between solid boundaries and fluid particles is solved by employing Dynamic Boundary Conditions (DBCs), as described in Crespo et al. (2007), which represents a very simple but robust method for incorporating fluid–solid interactions that are easy to use, even for very complex geometries. With this approach, solid boundaries consist of a set of particles that are treated as fluid particles, but their movement is constrained: the boundaries can be fixed or can move according to a particular forcing or motion time series. The Navier–Stokes equations are then applied to determine the interactions between boundary and fluid particles, imposing that the movement of the boundary particles is prescribed or equal to zero. When a fluid particle approaches a boundary particle, the fluid density locally increases, which in turn generates an increase in the pressure according to the equation of state (Eq. (5)) incorporated in WCSPH. The rise of pressure determines a repulsive force which avoids that fluid particles will pass through the boundary particles.

However, DBCs lead to over dissipation and consequent unphysical large boundary layers. Therefore, the so-called modified Dynamic Boundary Conditions (mDBCs) developed by English et al. (2022) are applied in the present work. Using mDBCs, the boundary particles are arranged similarly to DBCs, but the boundary interface is located at a distance proportional to the model resolution away from the innermost layer of boundary particles (defined as $dp/2$ for simple geometries). A ghost node is created in the fluid domain for each boundary particle, following the procedure described in Marrone et al. (2011). Each ghost node is projected towards the fluid domain according to the normal vector of the boundary pointing to the fluid. A simplified scheme is provided in Figure 3 of Altomare et al. (2021). While for a flat boundary, the projection is directed along the normal to the flat surface, for boundary particles located in corners, the normal for the projection is defined as the direction between the boundary particle and the corner. Once ghost nodes are projected, the fluid properties are then computed through a corrected SPH approximation. Finally, the properties calculated at the ghost nodes are mirrored back to the boundary particles.

In DualSPHysics, the user has the option to apply artificial viscosity to the fluid-boundary interaction. If this is not applied, the term representing this diffusion scheme in the momentum equation is neglected. This has been implemented to avoid unphysical damping effects at the interface between boundary and fluid, and it has been proven to be sensitive in some particular cases, such as in the propagation of bores or broken waves on gentle and long beaches (e.g. Domínguez et al., 2019).

For wave generation, DualSPHysics implements different schemes. Waves can be generated using boundary particles as moving boundaries (MB) that mimic the movement of a wavemaker in a physical facility. Long-crested second-order monochromatic waves, random sea states (including bound long waves), and solitary waves can all be automatically generated this way (Domínguez et al., 2019; Altomare et al., 2017). To absorb the reflected waves at the wavemaker and prevent the introduction of extra spurious energy in the fluid domain, an Active Wave Absorption System (AWAS) has been implemented in DualSPHysics (Altomare et al., 2017). The water surface elevation at the wavemaker position is used and transformed by an appropriate time-domain filter to obtain a control signal that corrects the wave paddle displacement in order to absorb the reflected waves every time step. The real-time position of the wavemaker is obtained through the velocity correction of its motion. As an alternative to MB, waves can

also be generated in DualSPHysics by enforcing the orbital velocity of the fluid particles in a specific generation area, using a Relaxation Zone method as described in Altomare et al. (2018) or by imposing fluid velocity and surface elevation in a buffer zone defined within an open boundary scheme (Verbrugghe et al., 2019). Other methods of wave generation include that of Tsuruta et al. (2021), where waves are generated by adjusting the position of the free surface in the generation zone by adding or removing particles, however this method is not yet implemented in DualSPHysics. In the present study, MBs with wedge-type wavemaker are employed.

3. Numerical and experimental set-up

Several numerical simulations have been conducted to determine the set-up that provided the best agreement between numerical results and experiments. In all the simulations the modified Dynamic Boundary Conditions (English et al., 2022) were adopted. Initially, both fluid and boundary particles are placed on the nodes of a $dp \times dp$ square lattice. The beach profile and the wedge-type wavemaker geometry have been imported as external *.vtk and *.stl files, respectively, and they are employed to fit the initial position of the boundary particles to the shape of the domain. The so-built boundary consists of a minimum of 5 particle layers, a number large enough to apply accurately both the density diffusion term correction and the modified Dynamic Boundary Conditions (mDBC). Notice that neither slip nor no-slip conditions are applied to the boundaries (not yet available in the latest version of DualSPHysics for complex geometries): instead, the velocity of the boundary particles is set equal to 0 as in the DBC scheme. Thresholds for density fluctuations are set in DualSPHysics: if the density of the fluid particles is exceeding the value of 1300 kg/m^3 or is smaller than 700 kg/m^3, the particle will be excluded from the simulation to prevent further numerical errors and instabilities. After a careful check, only a few particles (between 1 and 10 out of more than 1 million of particles) were excluded based on that criteria.

Waves have been generated by means of a moving boundary mimicking the experimental wedge-type wavemaker. Fluid particles have been created using the FILLBOX mode implemented in DualSPHysics, which fills the empty space within boundaries up to the target water depth. A variable time step is used based on the Courant–Friedrichs–Lewy condition, see Monaghan et al. (1999). DualSPHysics implements two different explicit time integration schemes. Here, the two-stage symplectic position Verlet time integrator scheme (Leimkuhler and Matthews, 2015) is employed.

It is important here to highlight that in SPH, there are two model resolutions that determine the final model accuracy (Rota-Roselli et al., 2018): (1) the interparticle distance dp that defines the total number of SPH particles (hence calculation points), but refers only to the discretization of the continuum into a finite number of elements placed on an initial regular lattice; (2) the smoothing length which defines the number of neighbouring particles used for calculation of all physical properties at each time step for each SPH particle. When referring to model performance and precision, a measure of the numerical error can be defined as the ratio between the smoothing length and significant quantities such as wave height, wave amplitude, run-up height, etc.

The phase-averaged x-velocity component was computed using Eq. (6),

$$\langle u \rangle = \frac{1}{N} \sum_{n=1}^{N} u\left[t + (n-1)T\right], \tag{6}$$

where $\langle u \rangle$ is the phase average of the x-velocity component ($0 \le t \le T$), T is the wave period, and N is the number of waves. Each simulation lasted 200 s but the first 60 s was removed from the time series because it was affected by the transient start-up effects. Since the wave period was 6 s, the phase-averaged velocities were based on $N = 23$ wave periods. The time-averaged x-velocity component $\bar{u}$, was calculated by averaging over an integer number of wave periods. The phase-averaged and time-averaged z-component of the velocity, $\langle w \rangle$ and $\overline{w}$, were calculated similarly.

The experiments were carried out in the large-scale CIEM wave flume at the Universitat Politècnica de Catalunya - Barcelona (Spain). Fig. 1 shows the experimental setup. The wave flume is 100 m long, 3 m wide and 4.5 m deep and is equipped with a wedge type wavemaker. The bottom profile was generated in a previous experiment (van der Zanden et al., 2016), and was subsequently made rigid by applying a layer of concrete. The bed profile consists of a bar with the offshore face sloping at 1:12 and the onshore face sloping at 1:4. The height of the bar, measured from the trough to the crest, was 0.65 m. Shoreward from the bar trough the bed slope was 1:125 for 10 m approximately and after which the profile ended with a 1:7 sloping beach approximately 8 m long.

The origin of the reference system lies on the still water level, at the position of the wavemaker at rest. The x-axis points in the onshore direction while the z-axis points vertically. The y spanwise axis has the origin on right channel wall, when facing the beach, and points towards the left wall. In all the experiments, the water depth at the wave paddle was 2.65 m. The wave conditions consisted of a monochromatic wave with period of 6 s and wave height $H = 0.55$ m.

The water surface elevation was measured at 54 unique cross-shore locations using resistive wave gauges (12 locations), acoustic wave gauges (27 locations) and pressure sensors (15 locations). The water surface elevation was obtained from pressure measurements by applying the linear wave theory. All these instruments measured at a sampling frequency of 40 Hz.

The velocity measurements were made using two laser Doppler anemometers (LDAs) and one acoustic Doppler velocimeter (ADV). Fig. 2 shows the position of the velocity measurement instruments.

The LDAs were two-component backscatter systems each powered by a 300 mW Ar-Ion air-cooled laser and equipped with a Dantec F60 Burst Spectrum Analyser. Each LDA was fitted with a 14 mm submersible probe with 50 mm focal length resulting in an ellipsoidal measuring volume with a maximum diameter of 115 μm and a length of 2 mm approximately in the y direction. The LDAs measure the u and w velocity components of particles that pass through the measuring volume, at a sampling rate that depends on the particle density and fluid velocity and varied between 150 Hz and 670 Hz. The ADV measured the three velocity components u, v and w at a sampling rate of 100 Hz in a cylindrical shaped measuring volume with diameter of 6 mm and length of 2.8 mm. These LDAs and ADV instruments were deployed from a frame attached to a carriage. The frame could be moved in the z-direction while the carriage in the x-direction so that the instruments could be positioned at specific (x, z) positions along the profile. The velocity measurements were carried out at 22 different cross-shore positions and for each of them three different elevations were covered by the frame, thus producing velocity measurements at 9 vertical positions (see Fig. 2). At each cross-shore position of the frame, waves were generated for approximately 45 min and measurements were obtained for a duration of 12 min at each elevation, corresponding to approximately 120 waves. For each measurement location, the velocities were averaged over no less than 100 wave periods. The phase- and time-averaged velocities were determined similarly to the SPH simulations.

To determine the best SPH simulation setup, several simulations have been performed to investigate the effect of key parameters on the ability of the model to reproduce the experiments. The parameters and results of all these simulations are shown in Appendix B together with a discussion of the results. The following set of parameters provided the best compromise between accuracy and computational cost: $dp = 1$ cm, ViscousBoundFactor (factor that multiplies α when calculating fluid boundary interaction, Barreiro et al., 2014)=0, coefh $= h_{SPH}/(dp\sqrt{2}) = 1.3$, $\alpha = 0.028$ and number of particles equal to 1.44×10^6. The value of 0.028 for α here adopted is significantly larger

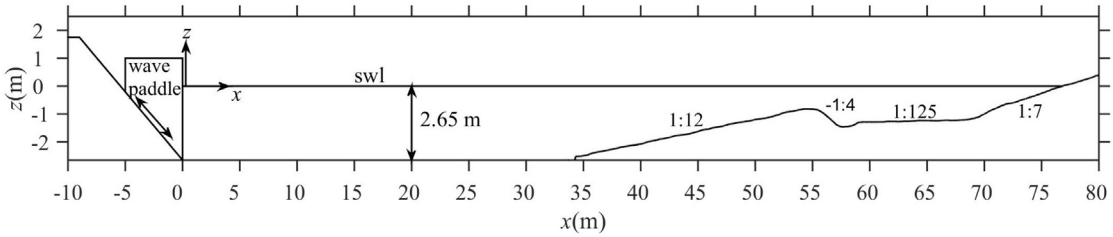

Fig. 1. Longitudinal profile of the wave flume.

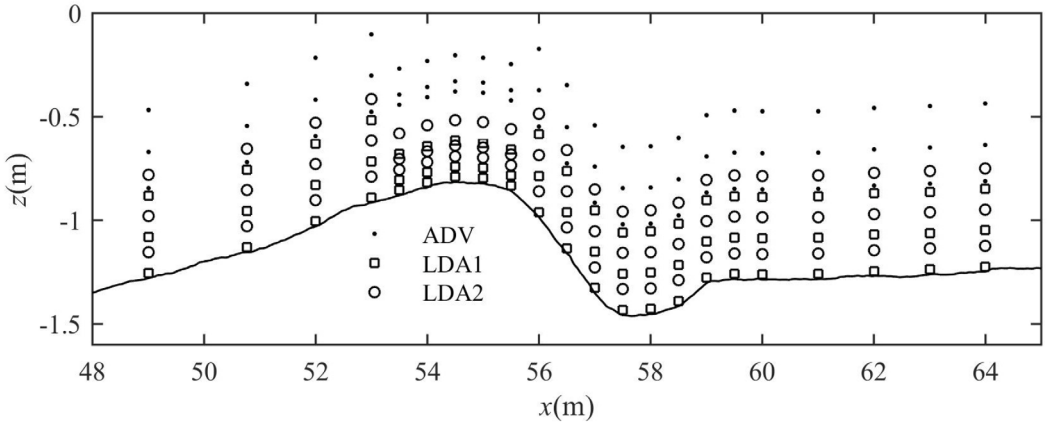

Fig. 2. Detail of the bar region showing the velocity measurement positions.

than 0.01 proposed by Altomare et al. (2015). This difference is likely due to the greater importance of the viscous effects for wave breaking, compared to the case of wave impacting on coastal structures studied in Altomare et al. (2015).

In literature, the spatial resolution for water waves is usually expressed as the number of particles used to resolve the offshore wave height and it is recommended to have $H_0/dp > 10$ (Rota-Roselli et al., 2018). This condition is fully satisfied in the present study since $H_0 =$ 0.55 m and $dp = 0.01$ m.

Despite the use of the density diffusion term by Fourtakas et al. (2019), the pressure and density fields are subject to fluctuations due to the explicit weakly compressible scheme adopted in DualSPHysics. Recently, two novel schemes have been proposed by Khayyer et al. (2023), referred to as the Velocity-divergence Error Mitigating (VEM) and the Volume Conservation Shifting (VCS), which will be implemented in future releases of DualSPHysics to improve the incompressibility condition and decrease the density fluctuations. However, despite the lack of a particularly sophisticated modelling approach, it was verified that the density variation in the present simulations remained below 0.3–0.4%, which is smaller than the maximum value of 1% considered acceptable. More detailed information on the density field fluctuations in the present simulations is given in Appendix C.

4. Comparison between SPH simulations and experiments

4.1. Water surface elevations

Fig. 3a shows the beach profile together with the position of the breaking and plunge points. The breaking point is the location where the free surface becomes vertical for the first time, due to the overturning process, while the plunge point is the location where the plunging jet hits the free surface. The surf similarity parameter (Battjes, 1974) for this wave condition is 0.84, which suggests a plunging breaker in agreement with the experimental observations.

When the jet plunges into the water column it produces a new wave which rapidly undergoes breaking. This breaking subsequently generates a new wave, which breaks again and then travels towards the shore as a bore. Fig. 3b shows the comparison between the average wave heights from the SPH simulation and those obtained through the experimental measurements. In the first 40 m of the channel the wave heights oscillate spatially, with an amplitude of approximately 0.12 m and a wavelength of 15 m. These oscillations are likely due to wave reflection from the beach, which generates a partial standing wave characterized by heights that vary in the x direction with a period that is half the length L of the incident wave, which was estimated to be $L = 30$ m in the horizontal part of the flume. Based on these observations, the estimated wave reflection coefficient is approximately 20%. In Fig. 3b, the numerical simulation shows good agreement with the experiments before the bar, where it also captures the oscillations, which indicates that the model correctly reproduces the reflection from the sloping beach. The maximum wave height near the breaking point is also reproduced with a fairly good accuracy.

In the breaking area, SPH predicts higher wave heights than most instruments. It is hard to judge whether this discrepancy is a numerical model overestimation, since it may be due to a difference in the definition of the free surface between wave gauges and the numerical model and to errors in the measuring system. These errors arise from the very complex dynamics of this region due to the water splashes and to the two-phase air/water mixture which produce flaws in measurement systems. The most critical locations in this respect are in $x = 52.82 - 57.78$ m, where the wave breaks generating the plunging jet which in turn gives rise to large splashes. This occurs in particular at $x = 57.78$ m where an acoustic and a resistive wave gauge along with a pressure sensor are placed. Fig. 3b shows that at this position these instruments produce different measurement values. In particular, the wave height from the acoustic wave gauge is significantly larger than that of the resistive wave gauge which, in turn, is only slightly larger than the wave height obtained from the pressure sensor. These differences are not necessarily due to malfunction, as the instruments are not based on the same operating principle and may therefore measure different values under critical conditions.

Pressure sensors use linear theory to extrapolate the height of the water surface. Therefore, when the non-linear effects induced by shoaling and breaking are significant, the pressure sensor estimates of the water surface elevation become less reliable. Acoustic wave gauges measure the bouncing time of the echo due to the impact of an acoustic pulse on the water surface. This technique is very accurate for smooth surfaces with gentle slopes, but for waves with steep slopes (waves before and during breaking) the echo of the acoustic pulse does not bounce to the emitter and a lot of data is missing. Resistive wave gauges, which evaluate free-surface elevation by measuring the electrical conductance between two parallel metal rods, are critically affected by splashing water and importantly they measure the upper free-surface including air pockets generated by the plunging breaker and this tends to distort the measure. Therefore, under conditions of large wave breaking, there is no method that can guarantee a very accurate measurement of wave height. This point has been previously raised by several researchers (Van Rijn et al., 2000; Marino et al., 2022; Astudillo et al., 2022).

Fig. 3c shows the absolute value of the difference between numerical and experimental average wave heights. As noted earlier, the most significant differences occur in the breaking region ($x = 54 - 63$ m) and mainly involve the pressure sensor and the resistive wave gauge measurements, which is probably because these instruments do not detect the large splashes occurring in this region, which are reproduced by SPH. The acoustic wave gauges, which measure from above, are better able to detect the splashes, which is probably why SPH is in better agreement with these measurements, with a maximum discrepancy of 0.13 m at $x = 66.8$ m.

Fig. 3d shows the standard deviation of the wave height based on 21 experiments. The largest standard deviation is 0.06 m and is recorded by the acoustic wave gauge placed at $x = 57.78$ m, just after the plunging point, where large wave-to-wave height variation is expected due to breaking. This result is probably due to the greater sensitivity of this instrument to large splashes. Considering that the maximum standard deviation is about 10% of the wave height, which only occurs at a few locations (see Fig. 3d), it can be said that the experiments did not show important variations of the wave height from wave to wave.

Figs. 4 and 5 show a comparison between the measured and SPH simulated phase-averaged free surface elevation at several positions along the flume for resistive and acoustic wave gauge measurements, respectively. Phase equal to zero corresponds to the zero upcrossing in time of the free surface at $x = 50.85$ m, where a resistive wave gauge is placed. In general, there is a reasonable agreement between experiments and numerical simulation although some notable discrepancies are also observed. Time-dependent water surface elevation exhibits shorter duration oscillations due to non-linearities which tend to generate higher order harmonics not always reproduced by SPH. These oscillations are absent for the first couple of waves after the start of wave generation, but they grow with time, attaining their final state after approximately 7 wave periods.

For example, in Fig. 4, at $x = 11.83$ m, the wavefront shows short period oscillations that are absent in the numerical simulation, although the wave height is correctly reproduced. These oscillations are also present at x = 28.54 m and at x = 47.21 m, but at these positions the numerical simulation follows the experimental measurements more closely. The Fourier transform of the free surface oscillations at $x = 11.83$ m shows that the amplitudes of the first three harmonic components of SPH and experiments are similar to each other, but the fourth component is significantly larger for the experiments. This is consistent with the results shown in Fig. 4 at t = 11.83 s, where the experimental measurements show 4 small oscillations during one wave period, that are not reproduced by SPH. These oscillations seem to be attenuated just before the wave break ($x = 50$–54 m), where the agreement between experiments and numerical simulations seems to improve. Due to the complexity of this flow, it is rather difficult to explain the exact origin of the differences between numerical simulations and experiments, as this would require further investigations beyond the scope of this paper.

Further differences in wave height are shown in the breaking region (see Fig. 4) at $x = 57.01$ m and $x = 58.21$ m. These discrepancies are due to the underestimation of the free surface elevation by the resistive wave gauges when they measure in the highly aerated water due to strong wave breaking as discussed above. On the other hand, the acoustic wave gauge measurements at $x = 57.78$ m (see Fig. 5), show a good agreement with SPH. This result echoes that shown in Fig. 3b, at $x = 57.78$ m where the wave height measured by the acoustic wave gauge shows a good agreement with the numerical result. Note that the wave height in Fig. 3b is not exactly the same as that inferred from Figs. 4 and 5. This is because the wave crest and trough do not occur exactly at the same phase at each wave period, hence the wave height deduced from Figs. 4 and 5 is generally slightly smaller than that shown in Fig. 3b. In Fig. 5, for $x \geq 66.79$ m there is a phase difference in the position of the wave crest between SPH and the experiments, which is about 0.35 s at $x = 71.1$ m. This phase difference occurs after the wave has undergone a complex physical transformation, due to breaking and to the secondary wave generated by the plunging jet, thus this small discrepancy seems acceptable.

4.2. Velocity distribution and pressure

Fig. 6 shows the experimental (left) and the numerical (right) phase-averaged velocity at 8 phases during the wave period. The experimental results include the phase-averaged free surface elevation for reference, since the velocity measurements do not cover the entire water column up to the free surface, like the SPH data. In all the panels the underlying contour plot shows the horizontal velocity component only.

At phase $t/T = 0$ the wave front is approaching the bar and breaking has not yet occurred. Similar results are provided by the numerical simulation which better highlights the velocity distribution along the entire water depth. At $t/T = 0.25$ the free surface is arranged vertically as the overturning of the wave front starts. At $t/T = 0.34$ the plunging jet hits the free surface and at phases 0.38–0.52 it enters the water column causing large downward velocities. After the jet has entered the water column, it causes a clockwise circulation on the trough of the bar that is clearly visible at the phases $t/T = 0.63$ and 0.875. This seems to agree with the experimental data, even though these do not clearly reveal a recirculating flow. It is expected that this recirculation cell constitutes one of the most important mechanisms influencing the growth of the bar when the bed is made up by mobile material. In general, there is a qualitative agreement between experiments and numerical simulation.

Numerical results show high velocities near the free surface, especially during wave breaking ($t/T = 0.34$). It is reported in the literature that the maximum velocity of water particles in plunging waves is of the order of the phase velocity. For example, Chang and Liu (1998) reported that the maximum velocity under plunging waves was 1.68 times the phase velocity. In this case, the phase velocity, estimated according to linear theory, is 5 m/s in the horizontal part of the wave channel and 3 m/s near the breaking point. Therefore, high water particle velocities as those shown in Fig. 6 are expected in the breaking region.

In the coastal region, the time-averaged velocity component plays an important role in the transport of sediments and pollutants. Therefore, providing information on the reliability of SPH modelling in reproducing this quantity is of practical importance for coastal engineering applications. Figs. 7 and 8 show the comparison between measured and predicted time-averaged velocity profiles. The agreement is fairly good both in the shoaling region and in the surf-zone. More significant differences are observed in the trough of the bar ($x = 57$–59.5 m) where the experiments show a strong gradient near the bed while SPH yields a milder gradient. In this area, the flow is influenced by the turbulence generated by the plunging jet, the effect of which

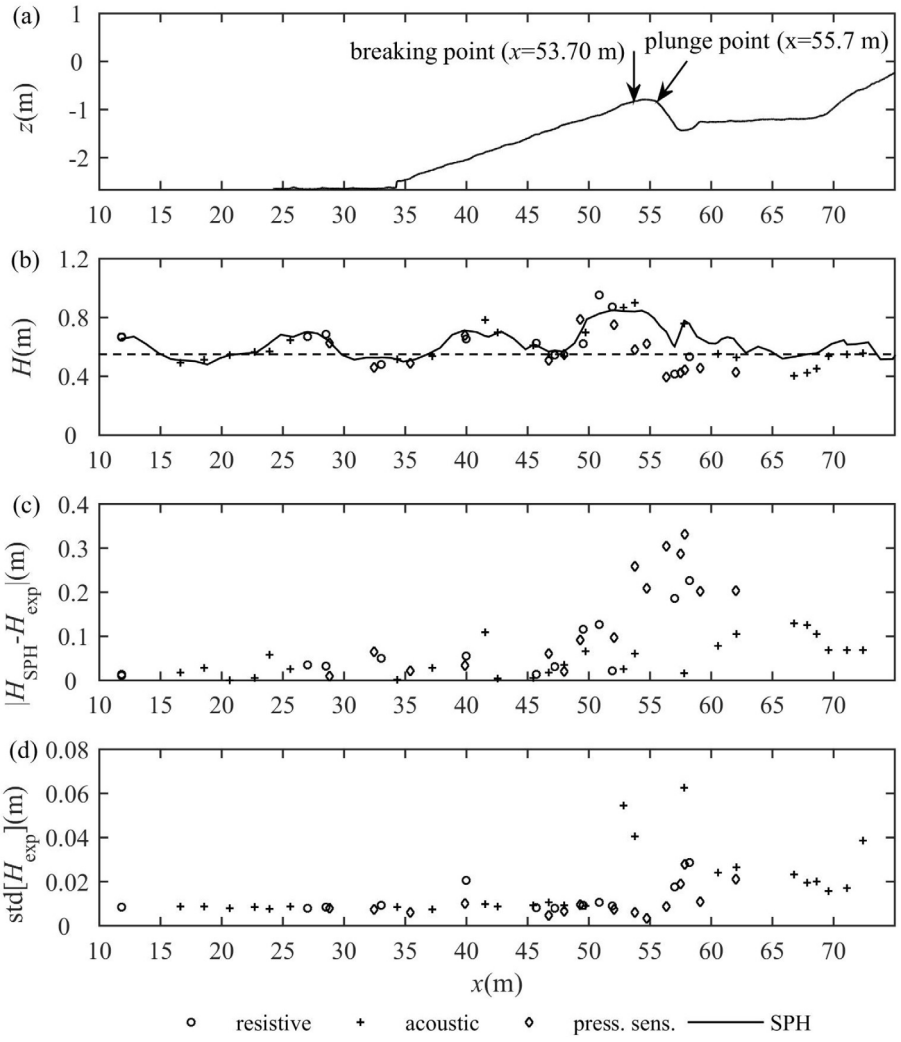

Fig. 3. (a) Bed profile; (b) average wave heights; (c) absolute value of the difference between SPH and experimental average wave heights; (d) standard deviation of the experimental wave heights.

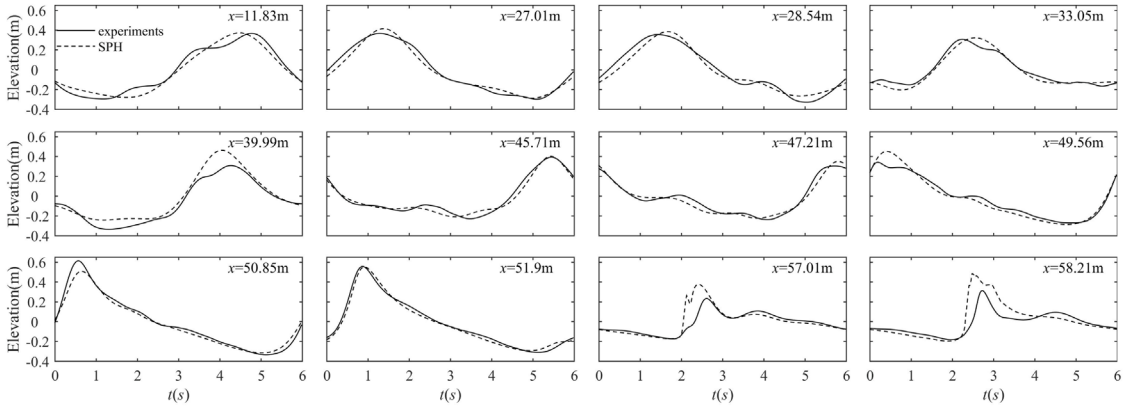

Fig. 4. Comparison between the measured and SPH predicted phase-averaged free surface elevation. Measurements based on the resistive wave gauges.

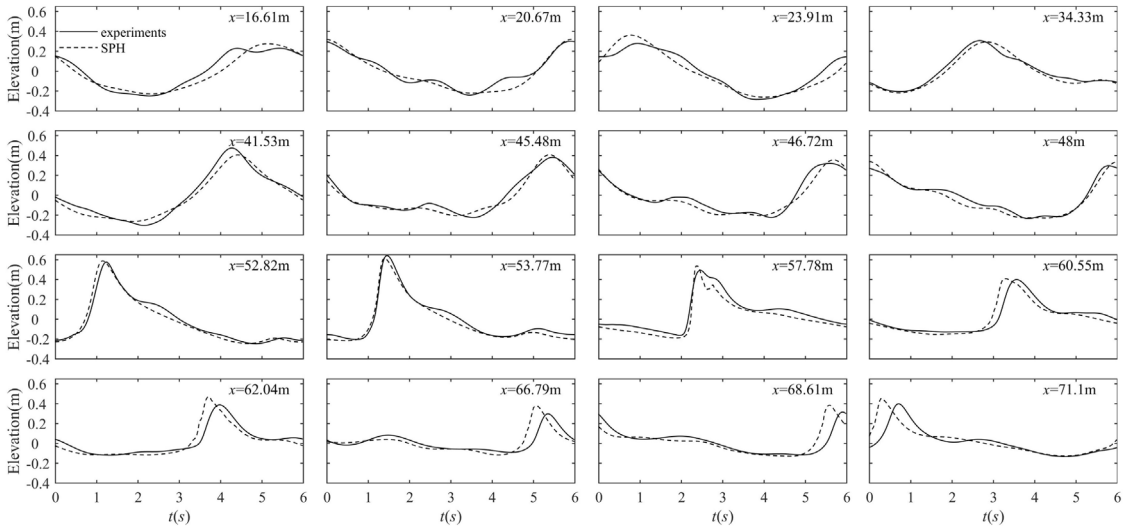

Fig. 5. Comparison between the measured and SPH predicted phase-averaged free surface elevation. Measurements based on the acoustic wave gauges.

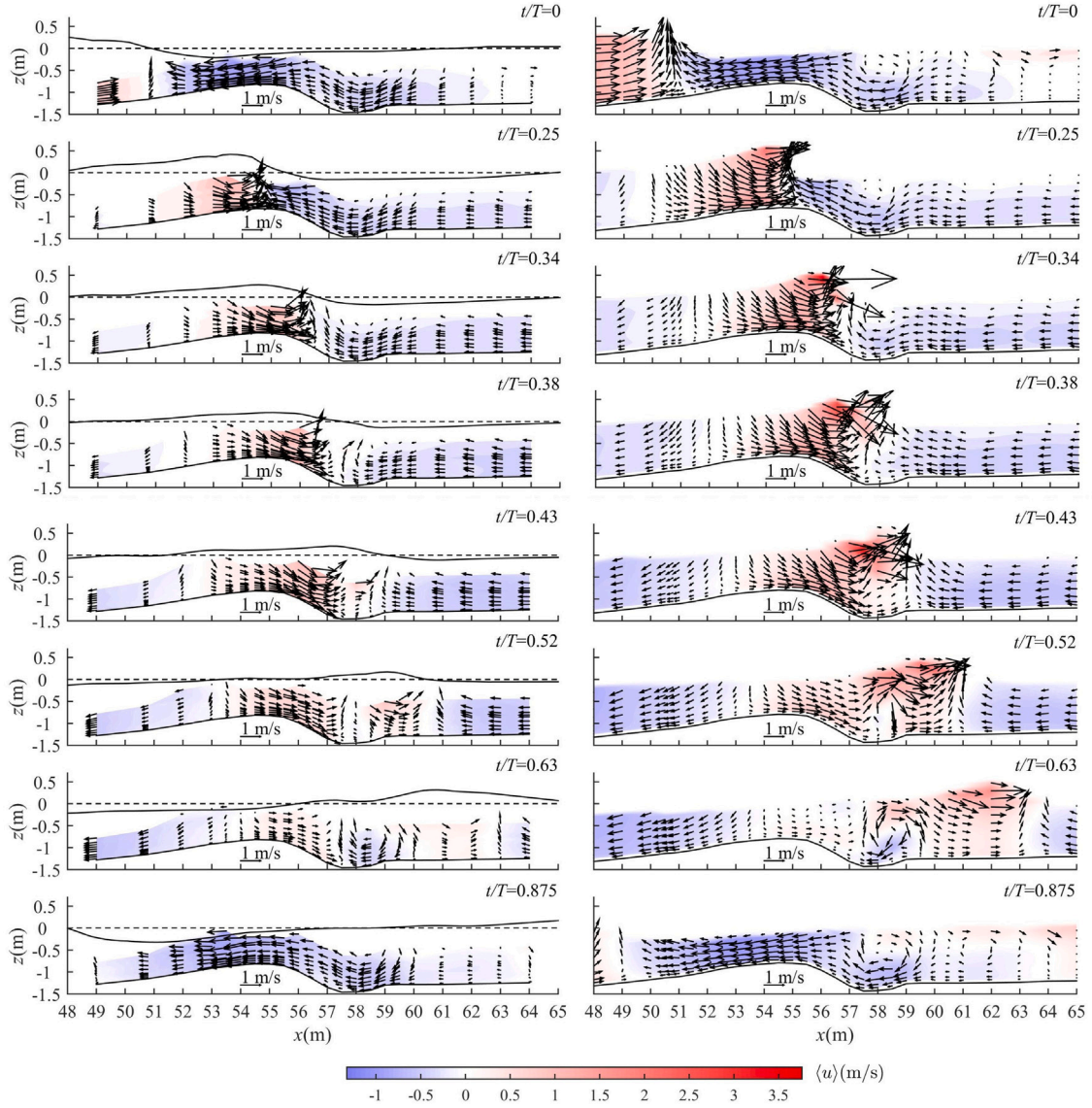

Fig. 6. Phase-averaged velocities; right column: experiments; left column: SPH. The colour contour represents the horizontal velocity component only.

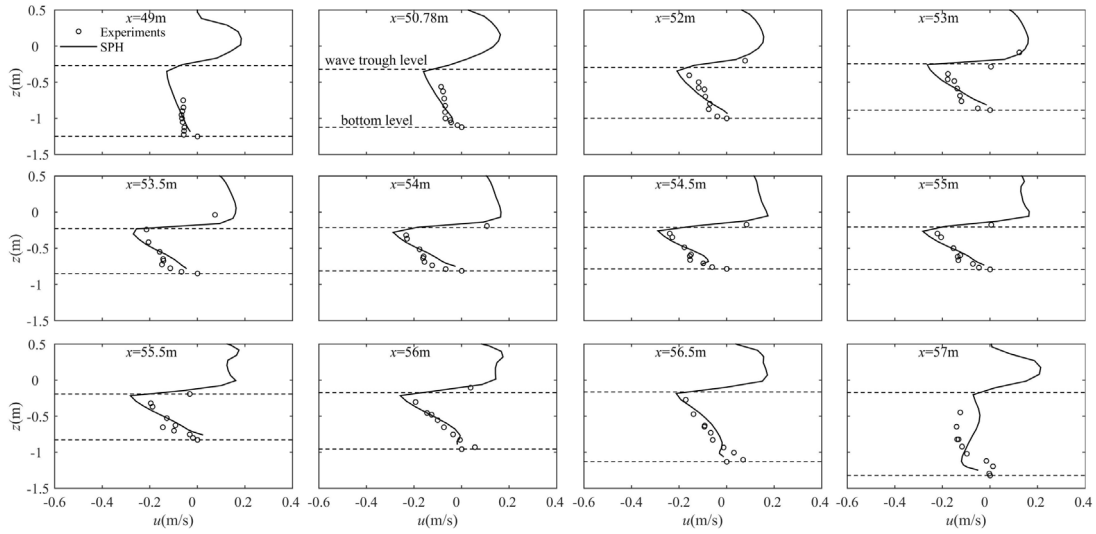

Fig. 7. Comparison between the time-averaged velocity profiles computed by means of SPH and those measured experimentally at $x = 49 - 57$ m.

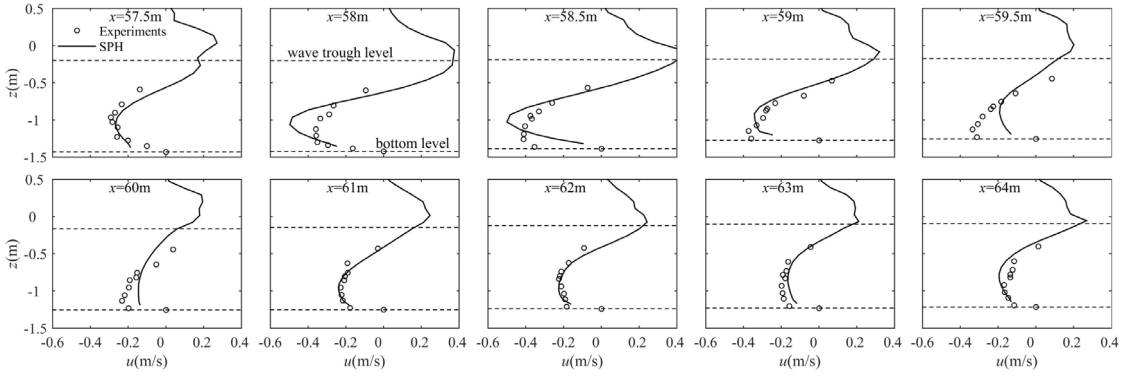

Fig. 8. Comparison between the time-averaged velocity profiles computed by means of SPH and those measured experimentally at $x = 57.5 - 64$ m.

would require more sophisticated models to be accurately reproduced. Despite these limitations, the flow is reproduced with acceptable accuracy onshore from the bar region, such as at $x = 61$ m, where turbulence still plays an important role.

The mean velocity is seaward directed in the lower part of the water column and onshore directed in the upper part. Generally, the elevation at which the time-averaged velocity changes direction is close to the wave trough in the shoaling region, whereas in the surf zone this change of direction occurs below the wave trough. Theory shows indeed that a Eulerian onshore mass transport occurs above the trough of the wave. Mass conservation will induce an offshore mass transport of the same magnitude, also known as undertow, which develops in the lower part of the water column.

Offshore from the breaking point ($x < 57$ m), at the elevation where the mean velocity changes sign, the velocity gradient is extremely large. At the same vertical positions in the surf zone ($x > 57.50$ m) the velocity gradient has more moderate values. This difference is mainly due to the turbulent mixing that characterizes the flow in the surf zone.

The time-averaged velocity profiles generated by wave propagation in this wave flume have been previously studied by Scandura and Foti (2011) who made measurements in the shoaling region on a sandy beach with a 1:15 slope for different wave conditions, some of which were not very different from those considered here. Due to the absence of a well-developed bar, in these experiments the waves broke at about $x = 67$ m, much further onshore than in the present case. A surprising result of these experiments was the detection of time-averaged velocity profiles with the convex side facing the shore, which in general is an unexpected situation. The most plausible, although not entirely exhaustive, explanation for this was the generation of offshore steady streaming in the bottom boundary layer due to asymmetric and/or skewed waves (see e.g., van der A et al., 2018). In Fig. 7 we observe a different picture with respect to this study as in the shoaling region the velocity distribution seems to follow a straight line. However, the findings of Scandura and Foti (2011) are not unique as they have also been reported by other studies (see references therein).

While the agreement of the present numerical results with the experiments is similar to that of Lowe et al. (2019), there are fundamental differences with respect to the previous study that should be highlighted. Lowe et al. (2019) reproduced small-scale waves breaking on a plane sloping beach, with water depth of 0.4 m in the horizontal part of the flume, wave height of 0.128 m and wave periods of 2 s or 5 s. On the other hand, current simulations concern large-scale waves breaking on a barred beach profile, for 2.65 m water depth in the horizontal part of the flume and wave height of 0.55 m, with a 6 s period, thus allowing to validate the model for wave and bed profile conditions much more similar to those found in the field.

Fig. 9a shows an overview of the time-averaged velocity distribution. The black lines in the upper part of this figure show the maximum (wave crest) and the minimum (wave trough) free surface elevation along the flume computed numerically. Offshore from $x \approx 57$ m, the mass transport is contained between the trough and the crest of the wave, as predicted by the linear wave theory, while onshore from this location the mass transport also extends below the wave trough. The most relevant feature of the average velocity distribution is the presence of a recirculating cell, in the bar through. The energy to keep this

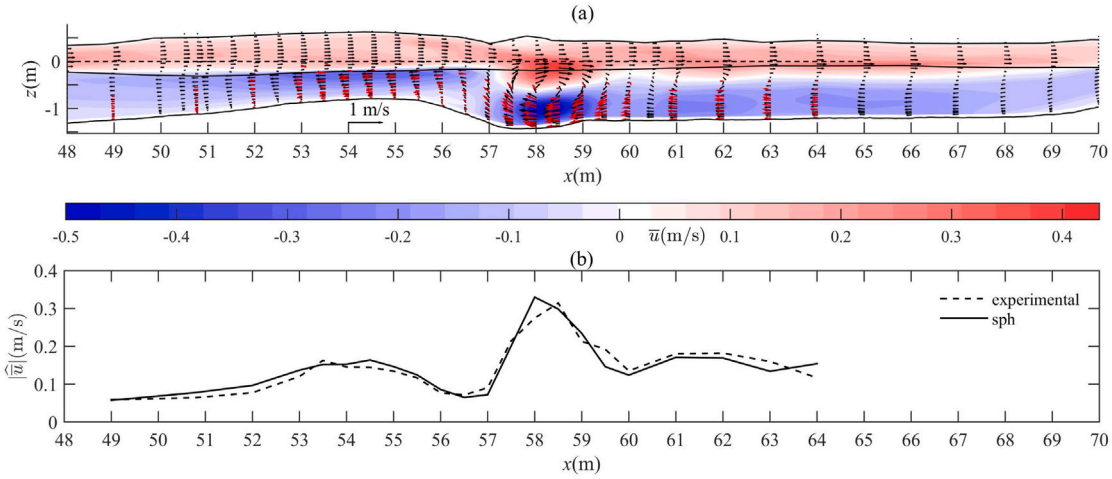

Fig. 9. (a) Time-averaged velocity distribution along the flume. Black arrows: experiments; Red arrows: SPH. The colour contour indicates the horizontal velocity component only; (b) absolute value of the vertical average, below the wave trough, over the z-range where experimental measurements are available, of the time-averaged horizontal velocity component, for both numerical and the experimental data.

recirculating flow is supplied by the wave breaking and in particular by the plunging jet that penetrates the water column transferring a large amount of momentum to depths which are close to the bed. At the most offshore shoaling zone locations, the mean velocity is small (−0.05 m/s on average in Fig. 9a) and almost uniform over the water depth, due to the convection which tends to homogenize the mean velocity distribution. An example of this behaviour is also shown in figure 1 of Scandura et al. (2012) where the mean velocity distribution over the depth was determined by solving the mean vorticity equation and compared with experimental measurements. The negative velocities increase shoreward, reaching values of −0.20 m/s at $x = 53.5$ m, where the overturning process begins. From here to $x = 56.5$ m the mean horizontal velocity slightly decreases in magnitude while it increases again up to the bar trough. It is at this position that maximum and minimum velocities are detected along the water column. Shorewards from $x = 60$ m, the velocity profile becomes more homogeneous again and remains rather constant along the lower part of the water column similarly to what was predicted and measured on the shoaling region. As already shown in the previous figures, the agreement between numerical results and experimental measurements is fairly good. To provide a simple way to quantitatively compare SPH and experimental velocities, Fig. 9b shows the absolute value of the vertically-averaged time-averaged velocities, over those elevations below the wave trough at which experimental measurements are available. This quantity is denoted as $|\hat{\overline{u}}|$, where the hat is used to indicate the vertical average. As noted earlier, the largest discrepancies occur at the onshore edge of the bar trough, while a reasonable agreement can be observed in the other locations.

Fig. 10 shows the onshore mass transport, denoted as MT, along the wave flume. For each of these positive mass transport values, a negative offshore mass transport of equal magnitude occurs in the lower part of the water column (not shown). The mass transport is rather constant in the shoaling region, though it slightly increases prior to breaking, attaining a maximum at around $x = 54$ m. Within 1 m in front of the plunge point the mass transport increases very rapidly, reaching a maximum in the middle of the bar trough after which it decreases rapidly reaching at the onshore edge of the bar trough a value that remains approximately constant in the surf zone. The mass transport is approximately 0.095 m^3/(m s) prior to breaking while, on average, it is 0.12 m^3/(m s) after breaking (x = 60–65 m). Thus, breaking causes an increase of 26% in this case. For linear waves, using the formula $MT = gH^2T/(8L)$, a value of 0.074 m^3/(s m) is obtained in the horizontal part of the flume, which is comparable to the numerical pre-breaking value. The large mass transport in the trough of the bar is due to the recirculating cell. The amount of recirculating flow can be estimated as the difference between the flow rate in the trough of the bar and the flow rate at the onshore edge of the trough, which provides 0.14 m^3/(m s), a value that is even larger than the mass transport in the surf zone.

Fig. 11 shows a comparison between the simulated pressure and the pressure measured by the pressure sensors. Since we used a weakly compressible SPH modelling approach, where the numerical speed of sound is significantly lower than the physical one in water (the ratio between the speed of sound and the maximum speed of the fluid, used in the simulation, is about 20), the pressure is affected by spurious oscillations due to acoustic waves travelling in the domain, having no physical origin. Therefore, following Meringolo et al. (2017), we used the Fourier transform to filter out the high-frequency fluctuations in the pressure before comparing it to pressure sensor data. As shown in Fig. 11, the general agreement between experiment and numerical simulation is acceptable, although there are some discrepancies.

Before concluding this section, it should be emphasized that in this flow the velocity in the spanwise direction (y-direction) is only due to the turbulence generated by the breaking and is generally weaker than in the other directions. This velocity component changes chaotically over time and its phase average vanishes. The current flow is therefore two-dimensional in the averaged sense. Nevertheless, 3D turbulent fluctuations can affect the properties of the 2D flow and could be at least partly responsible for the discrepancies between numerical and experimental results observed here. In order to keep into account these fluctuations, some simulations were carried out using the LES SPS based model (Gotoh et al., 2001), but the result did not improve with respect to the best one obtained using the artificial viscosity (see Appendix B where the results of several simulations are summarized). This lack of improvement is attributed to the modelling of the flow as 2D, because in order to correctly model the subparticles Reynolds stress, the flow must be considered as three-dimensional, which, in this case, would be prohibitively expensive given the size of the fluid domain and the hardware available. Other possible approaches to more rigorously include the effect of 3D fluctuations are those based on the solution of the Reynolds-averaged Navier–Stokes equations, which allow the calculation of the ensemble-averaged flow quantities distributed in two dimensions in this flow, but this would require the implementation of turbulence models such as the k-ϵ or k-ω models, which are not yet available in DualSPHysics.

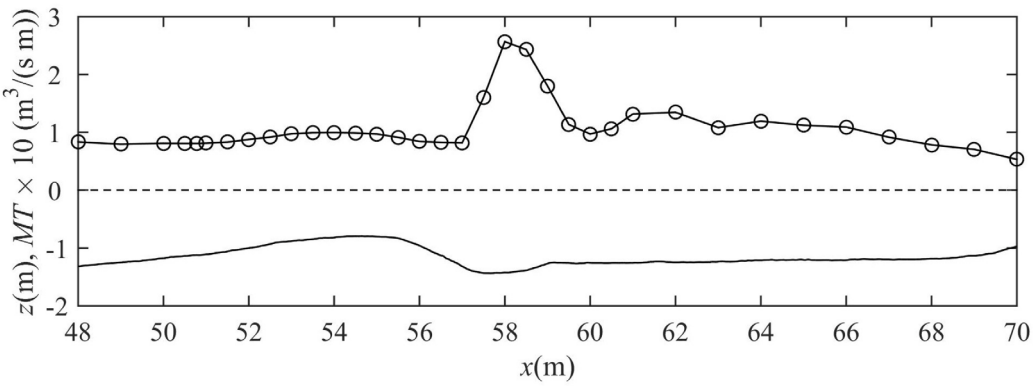

Fig. 10. Onshore mass transport obtained from the SPH simulation. The bottom line represents the bed profile.

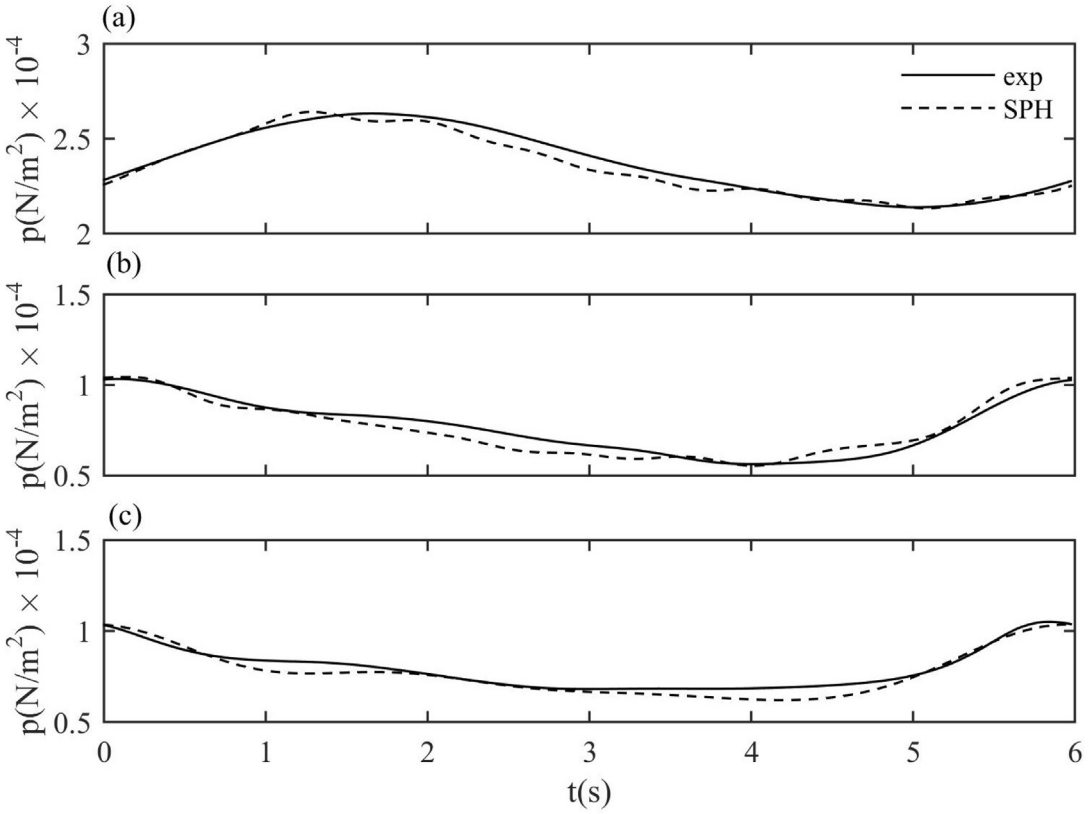

Fig. 11. Comparison between pressure measured by the pressure sensors and the filtered pressure from the SPH simulation. (a) x = 28.81 m, z = −2.40 m; (b) x = 48 m, z = −0.78 m; (c) x = 62.03 m, z = −0.78 m.

5. SPH numerical results and discussion

The analysis reported in this section is based only on the numerical simulation results as the experimental data are not suitable for describing the physical quantities under examination because they are not available over the entire water depth or are available on a too coarse grid.

5.1. Vorticity

Further insights into the physical processes related to wave breaking can be obtained by analysing the vorticity. This quantity, here denoted as ω, is the curl of the velocity field which in two dimensions is given by,

$$\omega = \frac{\partial w}{\partial x} - \frac{\partial u}{\partial z}. \tag{7}$$

The spatial resolution of the experimental data is too coarse to determine the velocity derivatives in Eq. (7) by means of the finite difference approximation. The reciprocal distance among the Lagrangian particles is on the other hand of the order of a centimetre, and this is sufficiently small to evaluate the velocity derivative using the kernel function, without incurring any significant errors. Therefore, the vorticity has been obtained from the numerical results only. Since the vortices generated by wave breaking follow different paths and occur in different sizes from wave to wave, phase averaging would tend to smooth out the boundary of the vortices so that they would no longer be recognizable in the fluid domain. Since the purpose of vorticity analysis is to obtain information on vortex dynamics, the instantaneous vorticity during a representative wave cycle is shown below.

Fig. 12 shows the vorticity at different phases during the 24th wave cycle in the wave time series. At $t/T = 0.26$ the wave front becomes almost vertical, with the wave starting to break off. At this instant, clockwise vorticity is mainly observed which is due to residues from the previous waves. At $t/T = 0.34$ the plunging jet hits the free surface and from this phase on vorticity will be strongly affected by breaking. There are three main mechanisms by which vorticity is generated after the plunging jet enters the water column and generates the large splash-up ($t/T = 0.40$):

i Vorticity is generated because of the strong curvature of the free surface within the cavity. In this case viscous fluid vorticity generation occurs even at the free surface because of the free shear stress boundary condition (Scandura et al., 2012).
ii A velocity discontinuity occurs between the plunging jet and the water that splashes up on the right. Because of this jump in velocity, counterclockwise vorticity is generated at this location ($t/T = 0.43$).
iii The velocity circulation around the cavity is generally different from zero. When the cavity collapses the Stokes circulation theorem shows that a flux of vorticity must be also generated. At $t/T = 0.43$ the cavity generated by the wave overturning can be seen, which produces clockwise vorticity, plus a cavity generated by the interaction between the plunging jet and the water that has splashed up, which produce counterclockwise vorticity.

After the collapse of all the cavities a vortex pair is generated which moves towards the bottom due both to the downward jet momentum and to the self-induced velocity. Due to the undertow current and also because the clockwise vortex is stronger than the counterclockwise one, the vortex pair turns to the left and resurfaces, causing a curvature of the free surface.

During the experiments the free surface buckling due to the vortex pair, shown at t/T=0.60–0.92, was observed in several occasions along with bubbles coming up towards the free surface. These bubbles where trapped within the cavities formed during wave breaking, and got carried towards the bottom due to the plunging jet, which was strong enough to overcome the buoyancy force, and were subsequently released when the vortex pair moved towards the top. The air bubbles at the bottom of the flume being driven by the vortex movement was measured and reported under similar conditions using Optical Backscatter Sensors (Cáceres et al., 2020).

In general, these vortex pairs were generated at every wave cycle following this mechanism, with some slight wave-to-wave differences, due to the variation in breaking process.

5.2. Energy spectra

It is interesting to verify whether the energy spectrum of this flow falls into one of the types described in literature. Fig. 13 shows the energy spectra $Sp_{u'u'}$ and $Sp_{w'w'}$ of the velocity fluctuations u' and w' respectively, based on SPH, at $(x, z) = (58.5, -0.34)$ m, in a region directly affected by breaking. Here u' and w' denote the difference between the instantaneous and the phase-averaged velocity (e.g. $u' = u - \langle u \rangle$). Note that these spectra are described in the angular wave-frequency space ($\sigma = 2\pi f$), where f is the frequency, while, usually, the spectra are presented in the wavenumber space. The two kinds of spectra are different from each other, but it was shown by Wilczek and Narita (2012) that their spectral index is the same. The difference between the two spectra lies in the constant of the spectral scaling law. A σ^{-3} power law can be seen extending from $\sigma = 7$ rad/s approximately towards large angular wave-frequency and a $\sigma^{-5/3}$ power law between $\sigma = 1$ rad/s approximately and $\sigma = 7$ rad/s. For $\sigma < 1$ rad/s the trend is not well defined and for this reason is difficult to be classified. These spectral ranges are similar to those reported in literature for a two dimensional turbulence (Lesieur, 1997). The σ^{-3} energy spectrum was predicted for two-dimensional isotropic turbulence by Kraichnan (1967) based on the classical theory of upward enstrophy cascade in wave-numbers space. The same theoretical framework predicts a $\sigma^{-5/3}$ range consistent with a downward energy cascade that is typical of two-dimensional turbulence. The peak in the spectrum is located at $\sigma = 1$ rad/s approximately, which corresponds to the angular wave-frequency of the incident wave. The wavenumber separating the enstrophy cascade from the inverse energy cascade is approximately 7 rad/s in this case. Following Kraichnan (1967), if the energy into the system is injected at a certain wavenumber (in practice in a narrow range of wavenumber), a spectrum similar to that shown in Fig. 13 is obtained, where the wavenumber of energy injection is at the boundary between the ranges $\sigma^{-5/3}$ and σ^{-3}. If this concept applies even to the present case an issue arises on the origin of the external forcing located at $\sigma = 7$ rad/s as the most obvious external forcing occurs at $\sigma = 1.047$ rad/s corresponding to the wave period of 6 s. The forcing at $\sigma = 7$ rad/s may be due to transfer of energy from the fundamental frequency ($\sigma = 1.047$ rad/s) to $\sigma = 7$ rad/s by the nonlinear effects, then this energy feeds the turbulent flow. This hypothesis requires a trough verification which goes beyond the scope of the present work.

5.3. Radiation stress

The depth-integrated and time-averaged momentum equation is often used to study coastal hydrodynamics. Generally, not all the terms of this equation are known, often they are parameterized based on experimental measurements, or they are derived from linear wave theory. The numerical data make it possible to obtain insight into these terms and highlight which of them are important and which not. The depth- and time-averaged momentum equation, neglecting bed shear stress, can be written as follows:

$$U\frac{\partial U}{\partial x} = -g\frac{\partial \overline{\eta}}{\partial x} - \frac{1}{\rho g(\overline{\eta} + h)}\frac{\partial S_{xx}}{\partial x}, \tag{8}$$

where U is the depth- and time-averaged velocity, $\overline{\eta}$ is the time-averaged free surface elevation, h is the local depth and S_{xx} is the radiation stress, which is the excess wave thrust per unit of width along

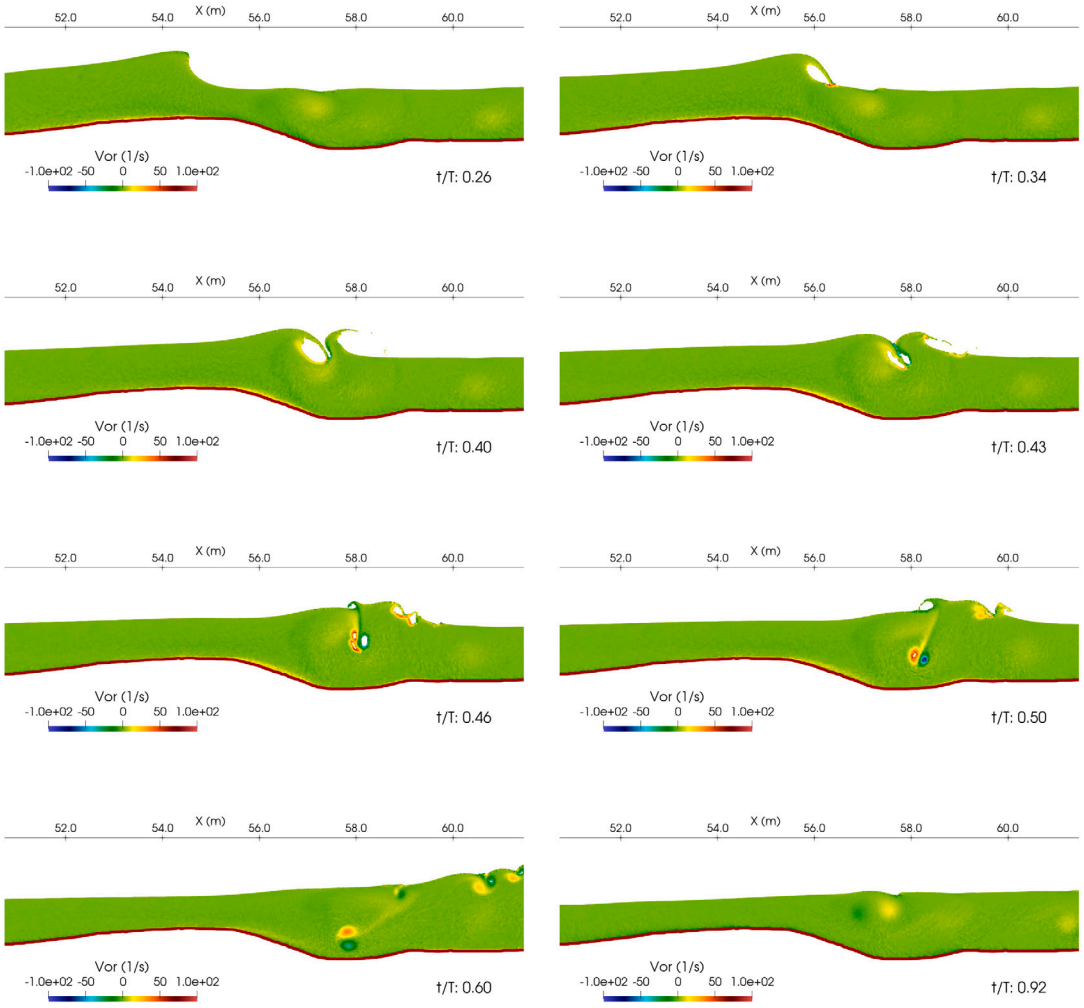

Fig. 12. Vorticity distribution obtained from the SPH simulation at selected phases during the 24th wave cycle.

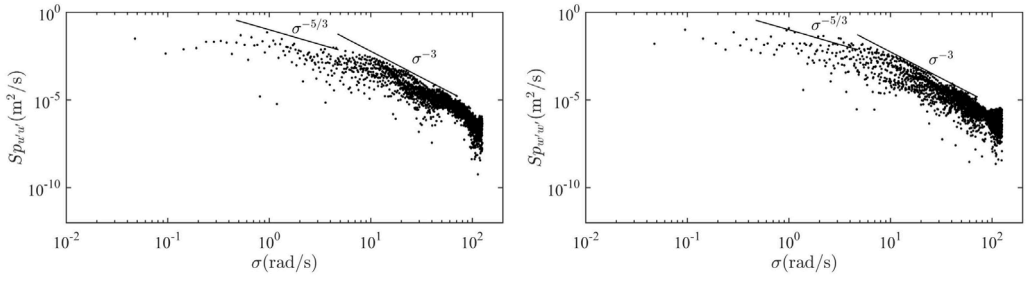

Fig. 13. Energy spectra of the fluctuating velocity components; left panel: cross-shore velocity component; right panel: vertical velocity component. $x = 58.5\,\mathrm{m}$, $z = -0.34\,\mathrm{m}$ (1.04 m from the bed).

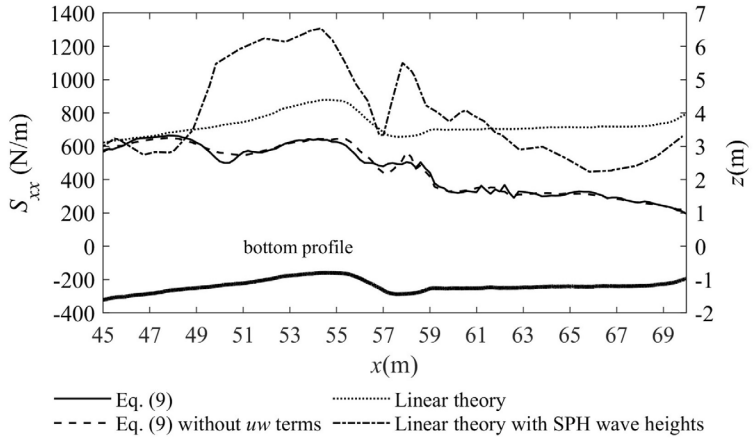

Fig. 14. Radiations stress S_{xx} along the flume obtained from: Eq. (9); Eq. (9) neglecting the 2nd and the 3rd terms (uw terms), and radiation stress computed according to the linear irrotational wave theory (Eq. (10)).

the water depth, with respect to the still condition. Taking into account equation 11.2.25 of Mei et al. (2005), which shows the expression of the radiation stress, and using equation 11.2.41, which is the expression of the time-averaged integral over the depth of the pressure, after applying Leibnitz's rule to the latter, the radiation stress can be written as shown in Eq. (9):

$$S_{xx} = \varrho g\overline{\frac{(\eta+h)^2}{2}} + \varrho\overline{\frac{\partial}{\partial x}\int_{-h}^{\eta}\left(\int_{z}^{\eta} uwdz\right)dz} - \varrho\frac{dh}{dx}\overline{\int_{-h}^{\eta} uwdz} - \varrho\overline{\int_{-h}^{\eta} w^2dz} + \varrho\overline{\int_{-h}^{\eta}\tilde{u}\tilde{u}dz} - \varrho g\frac{(\overline{\eta}+h)^2}{2} \tag{9}$$

where $\tilde{u} = u - U$ and a bar denotes a time average. For regular progressive waves on a gently sloping bottom the uw terms in Eq. (9) are often neglected leading for S_{xx} to equation (19) of Stive and Wind (1982). This approximation results from the fact that for periodic waves of permanent form u and w are 90° out of phase so that the time average of uw vanishes. However, in the present case this approximation is not expected to hold as the slope is not small and the waves undergo breaking. Furthermore, in some applications the radiation stress is estimated based on the linear irrotational wave theory as follows (Longuet-Higgins and Stewart, 1964):

$$S_{xx} = E\left(\frac{1}{2} + \frac{2kh}{sinh(2kh)}\right), \tag{10}$$

where E is the energy density ($E = \varrho g H^2/8$). Therefore, this section focuses on the verification of the importance of the uw terms in Eq. (9) and on the applicability of Eq. (10) to the present case. For the radiation stress based on Eq. (10), two different approaches have been adopted to determine the wave height H used to evaluate the energy density E. Using the first approach, H is evaluated by imposing a constant energy flux along the flume, while adopting the second, H is obtained from the SPH simulation. In both cases, the wavenumber k has been evaluated using the dispersion relationship, therefore, the difference between the two approaches is only due to the wave height.

Fig. 14 shows S_{xx} along the wave flume based on Eq. (9) and S_{xx} computed neglecting the uw terms in this equation. In addition, the radiation stress based on Eq. (10) is shown.

It can be observed that S_{xx} based on the SPH numerical simulation is approximately constant up to the crest of the bar and then decreases both because of the increase in depth and the energy dissipation which causes a reduction in wave height and momentum flux. As shown in Fig. 14, despite the occurrence of wave breaking, the radiation stress calculated without the uw terms is almost the same as that based on the full formula. However, to what extent this result is general cannot be established on the basis of this result only. Sufficiently offshore from the bar, the radiation stress based on the linear theory is close to the one provided by SPH as nonlinearities are weak at this position. On the crest of the bar the radiation stress based on the linear theory using the first approach (dotted line) is smaller than that computed using the second approach (dash-dotted line). This difference is due to the larger wave height produced by SPH simulation at this position due to wave reflection, which is not considered in the first approach, and also to nonlinearities. In general, linear wave theory, irrespective of the approach, significantly overestimates the radiation stress obtained from Eq. (9). This difference is because the linear wave theory does not account for energy dissipation, has difficulties in taking into account of wave reflection and disregards the undertow current.

Table B.1
Parameters of the simulations carried out for coefh = 1.3.

Simulation	dp (m)	α	Error (m/s)	E_v
1	0.04	0.01	0.083	0.5981
2		0.014	0.0415	0.3
3		0.02	0.0456	0.329
4		0.028	0.0665	0.479
5	0.02	0.01	0.0345	0.249
6		0.014	0.0363	0.261
7		0.02	0.0332	0.239
8		0.028	0.0341	0.246
9		Lam.+SPS	0.352	0.254
10	0.01	0.01	0.0239	0.172
11		0.014	0.0199	0.148
12		0.02	0.0198	0.143
13		0.028	0.0136	0.0978
14		Lam.+SPS	0.0285	0.2057
15	0.007	0.01	0.027	0.194
16		0.014	0.025	0.18
17		0.02	0.0228	0.164
18		0.028	0.0132	0.0951
19		Lam.+SPS	0.0217	0.1566

Table B.2
Parameters of the simulations carried out for dp = 0.01 m and coefh = 1.8 and 1.5.

Simulation	coefh	α	Error (m/s)	E_v
1	1.8	0.01	0.0422	0.304
2		0.014	0.047	0.267
3		0.02	0.0345	0.249
4		0.028	0.0323	0.233
5		lam.+SPS	0.0433	0.312
6	1.5	0.028	0.0215	0.1548

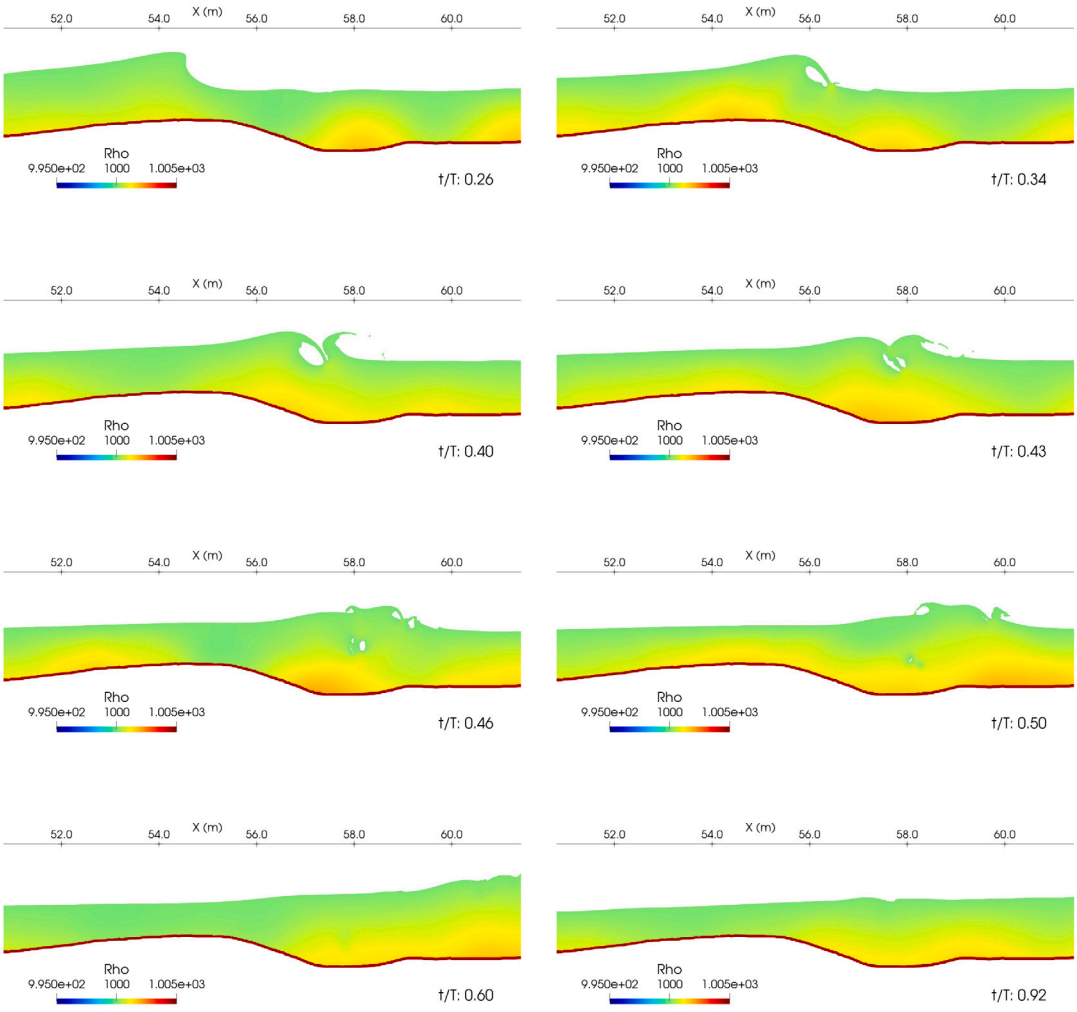

Fig. C.1. Density distribution obtained from the SPH simulation at selected phases during the 24th wave cycle.

6. Conclusions

SPH simulations of a large-scale plunging breaking wave on barred beach profile have been compared against new laboratory data with the aim of testing the numerical model and improving our understanding of the physical processes involving wave breaking. The present work represents an advancement on previous similar numerical studies which involved wave breaking in small-scale laboratory experiments with plane sloping beach profiles. Specifically, the advancement lies in the analysis of the hydrodynamics generated by wave breaking at a scale close to the natural one, thus allowing to significantly reduce the scale effects, so that the present results can be extrapolated to field conditions. The best agreement between the simulations and measurements was obtained with the following set of SPH parameters: coefh = 1.3 (ratio between the smoothing length and particle spacing), $\alpha = 0.028$ (artificial viscosity coefficient). The ratio between wave height H_0 in the horizontal part of the flume and the particle distance was 55. The ViscousBoundFactor, which is a specific parameter of the DualSPHysics solver used, has been set to 0.

Comparison between numerical results and experimental measurements has shown that present SPH-based model can properly forecast important features of the hydrodynamics of wave breaking such as the intra-wave free surface elevation and the time-averaged velocity field.

The predicted free surface elevation in the shoaling and surf zones is in a good agreement with the experimental measurements. Localized discrepancies occur where the plunging jet hits the free surface and generates a large splash up, which can be attributed to flaws in measurement systems in a region with a complex free surface and to model limitations. In this region the numerical results were in best agreement with the acoustic wave gauges.

The predicted time-averaged velocity along the wave flume is in a fairly good agreement with the experimental measurements, except at few locations, such as at the onshore end of the bar trough, where measurements show a larger velocity gradient near the bed. A recirculating flow is generated in the trough of the bar where the near bed velocity is directed towards the bar while away from the bed, the velocity is directed towards the shore. This velocity distribution is probably the basis of the mechanism by which the bar tends to grow in the case of a sandy bed.

The SPH simulation results were used to analyse physical quantities including vorticity, mass transport, energy spectra near the free surface, and the radiation stress, which could not be analysed using the experimental data.

The most prominent feature of the vorticity dynamics is the presence of a pair of vortices due both to the collapse of the cavity, induced by the wave overturning, and the interaction of the plunging jet with the water column. Within one wave period, these vortices travel downward and then veer off in offshore direction towards the bar, where they interact with the bed in the bar trough, and then move upwards towards the free surface.

In the region directly affected by breaking the energy spectrum has characteristics similar to a two-dimensional turbulence spectrum.

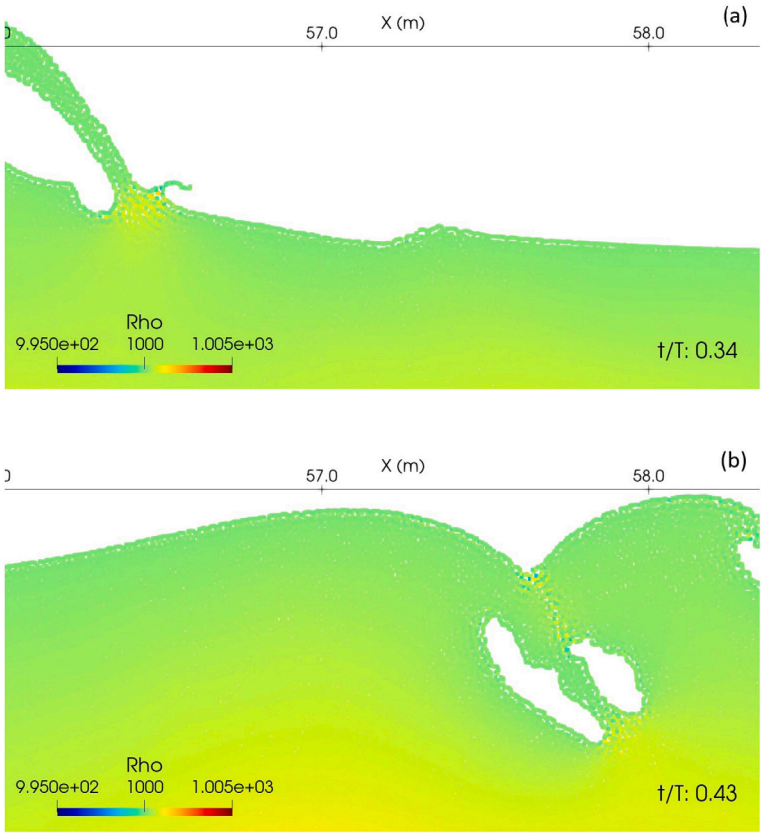

Fig. C.2. Close-up view of the density distribution in the neighbourhood of the impact of the plunging jet with free surface (a) and of the impact of the plunging jet with the splashed water (b) during the 24th wave cycle.

A $\sigma^{-5/3}$ range is detected at low angular wave-frequency due to the inverse energy cascade and a σ^{-3} direct energy cascade occurs at larger angular wave-frequency. The two spectral ranges border on each other at the angular wave-frequency of $\sigma = 7$ rad/s approximately. In the classical theory of two-dimensional turbulence the angular wave-frequency separating the two ranges is where the energy is injected into the system. How does this agree with the wave motion forced at an angular frequency of $\sigma = 1.05$ rad/s is not well understood and requires further research.

Mass transport in the shoaling region is rather constant with an average value of $0.095\,\mathrm{m}^3/(\mathrm{s\,m})$, while in the surf zone it increases by 26% as a result of wave breaking.

The radiation stress is rather constant offshore from the bar crest, and then decrease rapidly in the breaking region, because of the increase in water depth in the trough of the bar and energy dissipation, after which it decreases more gradually in the inner surf zone, mostly because of energy dissipation. The uw terms do not appear to be important when estimating the radiation stress. A more extensive study is needed to understand to what extend this result can be generalized. Sufficiently offshore from the bar, the radiation stress estimated from the linear wave theory is roughly in agreement with that determined from the SPH simulation, while in the breaking region linear theory leads to large discrepancies because it does not account for important processes including energy dissipation.

Before concluding, it is worth pointing out that although the current simulations were done in two dimensions, the real physics of this flow is three dimensional. Therefore, some observed discrepancies between numerical and experimental data may be due to the flow being considered two dimensional in the SPH simulation. However, taking into account the three-dimensionality of the waves generated in the current 3 m wide wave channel, and considering that the current two-dimensional simulation has used 1.44×10^6 particles, a three-dimensional simulation would require 423×10^6 particles in order to maintain the present spatial resolution, which would be prohibitively expensive with currently available hardware. Future works in this area should focus on improvements in modelling the effects of three-dimensionality within a two-dimensional approach to address the long-standing need for a reliable model for coastal zone hydrodynamics to be used for engineering applications.

CRediT authorship contribution statement

Corrado Altomare: Conceptualization, Methodology, Software, Formal analysis, Investigation, Writing – review & editing. **Pietro Scandura:** Conceptualization, Methodology, Software, Formal analysis, Investigation, Writing – original draft, Review & editing. **Iván Cáceres:** Conceptualization, Investigation, Writing – review & editing. **Dominic A. van der A:** Conceptualization, Investigation, Writing – review & editing. **Giacomo Viccione:** Conceptualization, Software, Investigation, Writing – review & editing.

Declaration of competing interest

The authors declare that they have no known competing financial interests or personal relationships that could have appeared to influence the work reported in this paper.

Data availability

Data will be made available on request

Acknowledgements

The experiments were supported by the European Community's Horizon 2020 Programme through the grant to the budget of the integrated infrastructure initiative HYDRALAB+, Contract no. 654110, and were conducted as part of the transnational access project HYBRID. Dr. Corrado Altomare acknowledges funding from the Spanish government and the European Social Found (ESF) under the programme 'Ramón y Cajal 2020' (RYC2020-030197-I/AEI/10.13039/501100011033). Pietro Scandura acknowledges the support received from the University of Catania, Italy by funding the research project 'Valutazione del rischio idraulico in sistemi complessi (VARIO)'.

Appendix A. Numerical code and experimental data availability

DualSPHysics is available for download at https://github.com/DualSPHysics/DualSPHysics/. Note that v5.0 is the version available online, while the present paper is based on v5.2 which will soon be publicly released. Experimental data are available upon request (van der Zanden et al., 2018).

Appendix B. Numerical simulations and effect of SPH parameters on accuracy of results

In order to gain insight into the effects of the artificial viscosity α, the spatial resolution dp and the coefh, and to determine the values of these parameters that provide a good compromise between accuracy and computational cost, several simulations were carried out, for parameter values given in Tables B.1 and B.2 for coefh = 1.3 and 1.8 respectively. In these simulations dp was varied in the range 0.007–0.04 m and α in the range 0.01–0.028. In addition, some simulations were carried out using the molecular viscosity of water and modelling the sub-particle Reynolds stress using Smagorinsky's eddy viscosity model (Laminar+SPS). The deviation of the numerical results from the experimental measurements was estimated by means of the dimensionless quantity E_v shown in the last column of each table. To determine E_v, the vertical average of the time-averaged velocities for both experiments ($V_{exp}(x)$) and numerical simulations ($V_{SPH}(x)$) was calculated over the depth at which experimental measurements are available. Then, the quantities $|V_{SPH}(x) - V_{exp}(x)|$ and $|V_{exp}(x)|$ were integrated over the x range covered by the experimental measurements and E_v was calculated as the ratio of the previous two integrals. Tables B.1 and B.2 also show the error in dimensional form given by the spatial average in the x direction of $|V_{SPH}(x) - V_{exp}(x)|$. For coefh = 1.3 and dp = 0.04 m, Table B.1 shows the minimum of the error at α = 0.014. Improving the resolution (dp = 0.02) E_v decreases and its minimum moves at α = 0.02. Further decreasing dp down to 0.01 m and 0.007 m the minimum is found at α = 0.028. In general, the error decreases as dp decreases. The results show that for coefh = 1.3 the best simulations are numbers 13 and 18, for which the errors are very similar to each other. Therefore, considering that simulation 18 is much more computationally expensive than simulation 13 due to

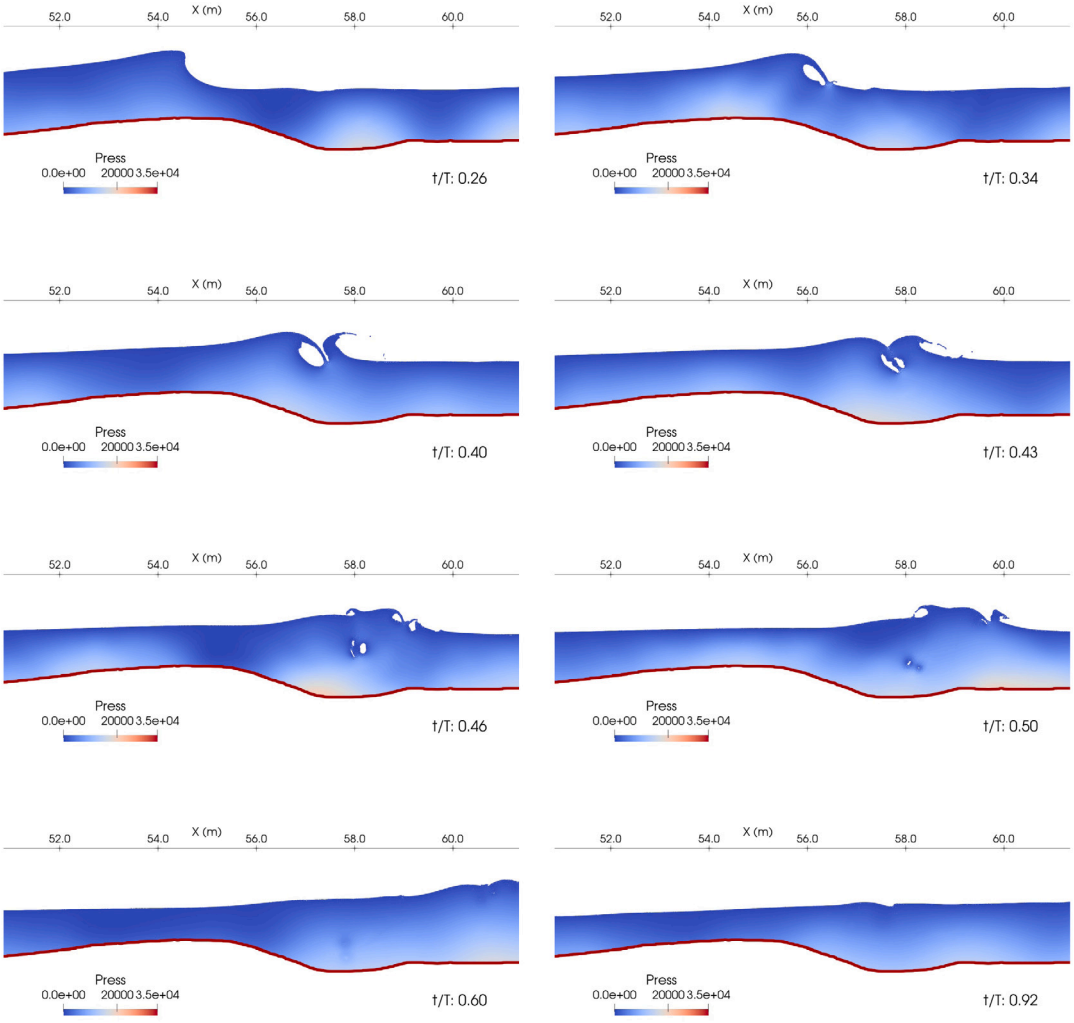

Fig. C.3. Pressure distribution obtained from the SPH simulation at selected phases during the 24th wave cycle.

the smaller value of dp, simulation 13 is chosen as the best case for coefh = 1.3. For coefh = 1.8 and 1.5 Table B.2 shows that the error decreases as α increases, but it always remains larger compared to the coefh = 1.3 conditions. As regards the simulation carried out with the SPS model, all the cases shown in Tables B.1 B.2 show that the errors are larger than in the best case carried out with the artificial viscosity, so case 13 of Table B.1 is finally adopted as the one that offers the best compromise in terms of model accuracy versus computational cost.

Appendix C. Density and pressure fields

Since the simulations in this study have been carried out using a weakly compressible SPH solver, it is important to show that the density variation during the wave cycle does not reach excessive values that could lead to dynamics significantly different from those of a nearly incompressible fluid. Fig. C.1 shows the fluid density distribution during a wave cycle, from which it can be seen that the density change from the reference value of 1000 kg/m^3 is contained within about 3–4 kg/m^3. This is a change of 0.3–0.4%, which is acceptable for present simulations to capture the correct dynamics. More importantly, the density field is spatially continuous in most regions of the domain. This can be seen by analysing the density field in regions where a density discontinuity is expected due to fluid impact, to show that any possible discontinuities are only confined to these regions. Fig. C.2(a) shows the density distribution near the region where the plunging jet hits the free surface at $t/T = 0.34$. Just around the impact region, the density varies in the range of approximately 1000–1001 kg/m^3. Particles with densities at these two extremes are located close to each other, indicating some density discontinuity in this region. However, this discontinuity is quite clearly caused by the impacting jet. As we move only a short distance away from this impact region, the density distribution becomes continuous. Fig. C.2(b) shows the density distribution where the plunging jet interacts with the splashed up water. Even in this case a density variation of approximately ± 1 kg/m^3 is observed along the impact surface, with the extreme values corresponding to locations that are close to each other. This can be considered as a discontinuity, but it is again limited to a small region where this may be justified. At a short distance away from the contact surface, the density is certainly continuously distributed.

Fig. C.3 shows the pressure distribution at the same phases of Fig. C.1. In this SPH model, the pressure is related to density by Tait's equation of state (see Eq. (5)). Therefore, the distribution of pressure is continuous if the density is also continuous. Previous discussion related to Figs. C.2 shows that possible discontinuities in density distribution are limited to small areas where plunging jet impact is observed and outside of these areas, the density is continuous. Therefore, we anticipate that the pressure is also continuous in the spatial domain, with the exception of the small areas where plunging jet impact occurs. We emphasize that the pressure distribution in Fig. C.3 does not provide as much information as the vorticity in Fig. 12. The only notable feature is that the vortex pair created by the plunging jet causes a localized decrease in pressure as can be seen at the phases $t/T = 0.50$ and $t/T = 0.60$.

References

Altomare, C., Crespo, A.J., Domínguez, J.M., Gironella, X., Gómez-Gesteira, M., 2014. Numerical modelling of armour block sea breakwater with smoothed particle hydrodynamics. Comput. Struct. 130, 34–35. http://dx.doi.org/10.1016/j.compstruc.2013.10.011.

Altomare, C., Crespo, A.J., Domínguez, J.M., Gómez-Gesteira, M., Suzuki, T., Verwaest, T., 2015. Applicability of smoothed particle hydrodynamics for estimation of sea wave impact on coastal structures. Coast. Eng. 96, 1–12. http://dx.doi.org/10.1016/j.coastaleng.2014.11.001.

Altomare, C., Domínguez, J.M., Crespo, A.J.C., González-Cao, J., Suzuki, T., Gómez-Gesteira, M., Troch, P., 2017. Long-crested wave generation and absorption for SPH-based DualSPHysics model. Coast. Eng. 127, 37–54. http://dx.doi.org/10.1016/j.coastaleng.2017.06.004.

Altomare, C., Gironella, X., Crespo, A.J.C., 2021. Simulation of random wave overtopping by a WCSPH model. Appl. Ocean Res. 116, 102888. http://dx.doi.org/10.1016/j.apor.2021.102888.

Altomare, C., Tafuni, A., Domínguez, J.M., Crespo, A.J.C., Gironella, X., Sospedra, J., 2020. SPH simulations of real sea waves impacting a large-scale structure. J. Mar. Sci. Eng. 8, 826. http://dx.doi.org/10.3390/jmse8100826.

Altomare, C., Tagliafierro, B., Domínguez, J.M., Suzuki, T., Viccione, G., 2018. Improved relaxation zone method in SPH-based model for coastal engineering applications. Appl. Ocean Res. 81, 15–33. http://dx.doi.org/10.1016/j.apor.2018.09.013.

Anthony, E.J., Aagaard, T., 2020. The lower shoreface: Morphodynamics and sediment connectivity with the upper shoreface and beach. Earth-Sci. Rev. 210, 103334. http://dx.doi.org/10.1016/j.earscirev.2020.103334, 32.

Astudillo, C., Gracia, V., Cáceres, I., Sierra, J., Sánchez-Arcilla, A., 2022. Beach profile changes induced by surrogate Posidonia Oceanica: Laboratory experiments. Coast. Eng. 175.

Barreiro, A., Domínguez, J.M., Crespo, A.J.C., González-Jorge, H., Roca, D., Gómez-Gesteira, M., 2014. Integration of UAV photogrammetry and SPH modelling of fluids to study runoff on real terrains. PLoS One 9 (11), e111031. http://dx.doi.org/10.1371/journal.pone.0111031.

Battjes, J.A., 1974. Surf similarity. In: Proceedings 14th International Conference on Coastal Engineering, Vol. 1. pp. 466–480. http://dx.doi.org/10.9753/icce.v14.26.

Cáceres, I., Alsina, J.M., Van der Zanden, J., Van der A., D.A., Ribberink, J., Sánchez-Arcilla, A., 2020. The effect of air bubbles on optical backscatter sensor measurements under plunging breaking waves. Coast. Eng. 159, 37–54. http://dx.doi.org/10.1016/j.coastaleng.2020.103721.

Chang, K.A., Liu, P.F., 1998. Velocity, acceleration and vorticity under a breaking wave. Phys. Fluids 10 (1), 327–329.

Crespo, A.J., Altomare, C., Domínguez, J., González-Cao, J., Gómez-Gesteira, M., 2017. Towards simulating floating offshore oscillating water column converters with smoothed particle hydrodynamics. Coast. Eng. 126, 11–26. http://dx.doi.org/10.1016/j.coastaleng.2017.05.001.

Crespo, A.J., Gómez-Gesteira, M., Dalrymple, R.A., 2007. Boundary conditions generated by dynamic particles in SPH methods. Comput. Mater. Cont. 5 (3), 173–184.

Dalrymple, R.A., Rogers, B.D., 2006. Numerical modeling of water waves with the SPH method. Coast. Eng. 53 (2), 141–147. http://dx.doi.org/10.1016/j.coastaleng.2005.10.004.

De Padova, D., Brocchini, M., Buriani, F., Corvaro, S., De Serio, F., Mossa, M., Sibilla, S., 2018. Experimental and numerical investigation of pre-breaking and breaking vorticity within a plunging breaker. Water 10 (387), 17. http://dx.doi.org/10.3390/w10040387.

Domínguez, J.M., Altomare, C., Gónzalez-Cao, J., Lomonaco, P., 2019. Towards a more complete tool for coastal engineering: solitary wave generation, propagation and breaking in an SPH-based model. Coast. Eng. J. 61, 15–40. http://dx.doi.org/10.1080/21664250.2018.1560682.

Domínguez, J.M., Crespo, A.J.C., Valdez-Balderas, D., Rogers, B.D., Gómez-Gesteira, M., 2013. New multi-GPU implementation for smoothed particle hydrodynamics on heterogeneous clusters. Comput. Phys. Comm. 184 (1), 1848–1860. http://dx.doi.org/10.1016/j.cpc.2013.03.008.

Domínguez, J.M., Fourtakas, G., Altomare, C., Canelas, R.B., Tafuni, A., García-Feal, O., Martínez-Estévez, I., Mokos, A., Vacondio, R., Crespo, A.J.C., Rogers, B.D., Stansby, P.K., Gómez-Gesteira, M., 2022. DualSPHysics: from fluid dynamics to multiphysics problems. Comput. Part. Mech. 9 (5), 867–895. http://dx.doi.org/10.1007/s40571-021-00404-2.

Dubarbier, B., Castelle, B., Ruessink, G., Marieu, V., 2017. Mechanisms controlling the complete accretionary beach state sequence. Geophys. Res. Lett. 44 (11), 5645–5654. http://dx.doi.org/10.1002/2017GL073094.

Elsayed, S.M., Gijsman, R., Schlurmann, T., Goseberg, N., 2022. Nonhydrostatic numerical modeling of fixed and mobile barred beaches: Limitations of depth-averaged wave resolving models around sandbars. J. Waterw. Port Coast. Ocean Eng. 148, http://dx.doi.org/10.1061/(ASCE)WW.1943-5460.0000685.

English, A., Domínguez, J.M., Vacondio, R., Crespo, A.J.C., Stansby, P.K., Lind, S.J., Chiapponi, L., Gómez-Gesteira, M., 2022. Modified dynamic boundary conditions (mDBC) for general purpose smoothed particle hydrodynamics (SPH): application to tank sloshing, dam break and fish pass problems. Comput. Part. Mech. 9 (5), 911–925. http://dx.doi.org/10.1007/s40571-021-00403-3.

Farahani, R.J., Dalrymple, R.A., Hérault, A., Bilotta, G., 2013. Three-dimensional SPH modeling of a bar/rip channel system. J. Waterw. Port Coast. Ocean Eng. 140 (1), 82–99. http://dx.doi.org/10.1061/(ASCE)WW.1943-5460.0000214.

Fourtakas, G., Domínguez, J.M., Vacondio, R., Rogers, B.D., 2019. Local uniform stencil (LUST) boundary condition for arbitrary 3-D boundaries in parallel smoothed particle hydrodynamics (SPH) models. Comput. & Fluids 190 (15), 346–361. http://dx.doi.org/10.1016/j.compfluid.2019.06.009.

González-Cao, J., Altomare, C., Crespo, A., Domínguez, J., Gómez-Gesteira, M., Kisacik, D., 2019. On the accuracy of DualSPHysics to assess violent collisions with coastal structures. Comput. & Fluids 179, 604–612. http://dx.doi.org/10.1016/j.compfluid.2018.11.021.

Gotoh, H., Khayyer, A., 2018. On the accuracy of DualSPHysics to assess violent collisions with coastal structures. Coast. Eng. J. 60, 79–103. http://dx.doi.org/10.1080/21664250.2018.1436243.

Gotoh, H., Shibahara, T., Sakai, T., 2001. Sub-particle-scale turbulence model for the MPS method - Lagrangian flow model for hydraulic engineering. Comput. Fluid Dyn. 9 (4), 339–347.

Grilli, S.T., Guyenne, P., Dias, F., 2001. A fully non-linear model for three-dimensional overturning waves over an arbitrary bottom. Internat. J. Numer. Methods Fluids 35, 829–867.

Hughes, T.P., Kerry, J.T., Baird, A.H., Connolly, S.R., Dietzel, A., Eakin, C.M., Heron, S.F., Hoey, A.S., Hoogenboom, M.O., Liu, G., McWilliam, M.J., Pears, R.J., Pratchett, M.S., Skirving, W.J., Stella, J.S., Torda, G., 2018. Global warming transforms coral reef assemblages. Nature 556 (7702), 492–496. http://dx.doi.org/10.1038/s41586-018-0041-2.

Jacobsen, G.N., Fredsøe, J., Jensen, J.H., 2014. Formation and development of a breaker bar under regular waves. Part 1: Model description and hydrodynamics. Coast. Eng. 88, 182–193. http://dx.doi.org/10.1016/j.coastaleng.2013.12.008.

Kelebek, M.B., Batibeniz, F., Önol, B., 2021. Exposure assessment of climate extremes over the Europe-mediterranean region. Atmosphere 12 (5), 633. http://dx.doi.org/10.3390/atmos12050633.

Khayyer, A., Gotoh, H., Falahaty, H., Shimizu, Y., 2018. An enhanced ISPH–SPH coupled method for simulation of incompressible fluid-elastic structure interactions. Comput. Phys. Comm. 232, 139–164. http://dx.doi.org/10.1016/j.cpc.2018.05.012.

Khayyer, A., Shimizu, Y., Gotoh, T., Gotoh, H., 2023. Enhanced resolution of the continuity equation in explicit weakly compressible SPH simulations of incompressible free-surface fluid flows. Appl. Math. Model. 116, 84–121. http://dx.doi.org/10.1016/j.apm.2022.10.037.

Kraichnan, R.H., 1967. Inertial ranges in two-dimensional turbulence. Phys. Fluids 10, 1417–1423.

Lee, W.K., Tay, S.H.X., Ooi, S.K., Friess, D.A., 2021. Potential short wave attenuation function of disturbed mangroves. Estuar. Coast. Shelf Sci. 248, 106747. http://dx.doi.org/10.1016/j.ecss.2020.106747.

Leimkuhler, B., Matthews, C., 2015. Molecular Dynamics: With Deterministic and Stochastic Numerical Methods. Springer.

Lesieur, M., 1997. Turbulence in Fluids. Springer Dordrecht, http://dx.doi.org/10.1007/978-94-010-9018-6.

Longuet-Higgins, M.S., Stewart, R.W., 1964. Radiation stress in water waves; a physical discussion with applications. Deep-Sea Res. 11, 529–562.

Lowe, R.J., Altomare, C., Buckley, M., da Silva, R.F., Hansen, J.E., Rijnsdorp, D., Domínguez, J.M., Crespo, A.J.C., 2022. Smoothed particle hydrodynamics simulations of reef surf zone processes driven by plunging irregular waves. Ocean Model. 171, 101945. http://dx.doi.org/10.1016/j.ocemod.2022.101945.

Lowe, R.J., Buckley, M.L., Altomare, C., Rijnsdorp, D.P., Yao, Y., Suzuki, T., Bricker, J.D., 2019. Numerical simulations of surf zone wave dynamics using smoothed particle hydrodynamics. Ocean Model. 144, 101481. http://dx.doi.org/10.1016/j.ocemod.2019.101481.

Lucy, L.B., 1977. A numerical approach to the testing of the fission hypothesis. Astron. J. 82, 1013–1024. http://dx.doi.org/10.1086/112164.

Lupieri, G., Contento, G., 2015. Numerical simulations of 2-D steady and unsteady breaking waves. Ocean Eng. 106, 298–316. http://dx.doi.org/10.1016/j.oceaneng.2015.07.014, 3259.

Makris, C.V., Memos, C.D., Krestenitis, Y.N., 2016. Numerical modeling of surf zone dynamics under weakly plunging breakers with SPH method. Ocean Model. 98, 12–35. http://dx.doi.org/10.1016/j.ocemod.2015.12.001.

Marino, M., Cáceres, I., Musumeci, R., 2022. Measuring free surface elevation of shoaling waves with pressure transducers. Cont. Shelf Res. 245.

Marrone, S., Antuono, M., Colagrossi, A., Colicchio, G., Le Touzé, D., Graziani, G., 2011. δ-SPH model for simulating violent impact flows. Comput. Methods Appl. Mech. Engrg. 200 (13-16), 1526–1542.

Mei, C.C., Stiassnie, M., Yue, D.K.P., 2005. Theory and Application of Ocean Surface Wave. Part 2: Nonlinear Aspects. World Scientific Publishing.

Meringolo, D., Colagrossi, A., Marrone, S., Aristodemo, F., 2017. On the filtering of acoustic components in weakly-compressible SPH simulations. J. Fluids Struct. 70, 1–23. http://dx.doi.org/10.1016/j.jfluidstructs.2017.01.005.

Meringolo, D., Liu, Y., Wang, X., Colagrossi, A., 2018. Energy balance during generation, propagation and absorption of gravity waves through the δ-LES-SPH model. Coast. Eng. 140, 355–370. http://dx.doi.org/10.1016/j.coastaleng.2018.07.007.

Monaghan, J.J., 1985. Particle methods for hydrodynamics. Comput. Phys. Rep. 3 (2), 71–124. http://dx.doi.org/10.1016/0167-7977(85)90010-3.

Monaghan, J.J., 1992. Smoothed particle hydrodynamics. Annu. Rev. Astron. Astrophys. 30, 543–574. http://dx.doi.org/10.1146/annurev.aa.30.090192.002551.

Monaghan, J.J., 1994. Simulating free surface flows with SPH. J. Comput. Phys. 110, 399–406. http://dx.doi.org/10.1006/jcph.1994.1034.

Monaghan, J., Cas, R., Kos, A., Hallworth, M., 1999. Gravity currents descending a ramp in a stratified tank. J. Fluid Mech. 379, 39–70.

Oger, G., Doring, M., Alessandrini, B., Ferrant, P., 2007. An improved SPH method: Towards higher order convergence. J. Comput. Phys. 225 (2), 1472–1492. http://dx.doi.org/10.1016/j.jcp.2007.01.039.

Pelosi, A., Furcolo, P., Rossi, F., Villani, P., 2020. The characterization of extraordinary extreme events (EEEs) for the assessment of design rainfall depths with high return periods. Hydrol. Process. 34 (11), 2543–2559. http://dx.doi.org/10.1002/hyp.13747.

Rafati, Y., Hsu, T.J., Elgar, S., Raubenheimer, B., Quataert, E., van Dongeren, A., 2021. Modeling the hydrodynamics and morphodynamics of sandbar migration events. Coast. Eng. 166, 103885. http://dx.doi.org/10.1016/j.coastaleng.2021.103885.

Rota-Roselli, R.A., Vernengo, G., Altomare, C., Brizzolara, S., Bonfiglio, L., Guercio, R., 2018. Ensuring numerical stability of wave propagation by tuning model parameters using genetic algorithms and response surface methods. Environ. Model. Softw. 103, 62–73. http://dx.doi.org/10.1016/j.envsoft.2018.02.003.

Ruessink, B.G., Blenkinsopp, C., Brinkkemper, J.A., Castelle, B., Dubarbier, B., Grasso, F., Puleo, J.A., Lanckriet, T., 2016. Sandbar and beach-face evolution on a prototype coarse sandy barrier. Coast. Eng. 113, 19–32. http://dx.doi.org/10.1016/j.coastaleng.2015.11.005.

Scandura, P., Foti, E., 2011. Measurements of wave-induced steady currents outside the surf zone. J. Hydraul. Res. 49 (sup1), 64–71. http://dx.doi.org/10.1080/00221686.2011.591046.

Scandura, P., Foti, E., Faraci, C., 2012. Mass transport under standing waves over a sloping beach. J. Fluid Mech. 701, 460–472. http://dx.doi.org/10.1017/jfm.2012.181.

Shao, S., Ji, C., Graham, D.I., Reeve, D.E., James, P.W., Chadwick, A.J., 2006. Simulation of wave overtopping by an incompressible SPH model. Coast. Eng. 53 (9), 723–735. http://dx.doi.org/10.1016/j.coastaleng.2006.02.005.

Stive, M.J.F., Wind, H.G., 1982. A study of radiation stress and set-up in the nearshore region. Coast. Eng. 6, 1–25.

Suzuki, T., García-Feal, O., Domínguez, J.M., Altomare, C., 2022. Simulation of 3D overtopping flow-object-structure interaction with a calibration-based wave generation method with DualSPHysics and SWASH. Comput. Part. Mech. 9 (5), 1003–1015. http://dx.doi.org/10.1007/s40571-022-00468-8.

Tazaki, T., Harada, E., Gotoh, H., 2022. Numerical investigation of sediment transport mechanism under breaking waves by DEM-MPS coupling scheme. Coast. Eng. 175, 19. http://dx.doi.org/10.1016/j.coastaleng.2022.104146.

Tissier, M., Bonneton, P., Marche, F., Chazel, F., Lannes, D., 2012. A new approach to handle wave breaking in fully non-linear Boussinesq models. Coast. Eng. 67, 54–56. http://dx.doi.org/10.1016/j.coastaleng.2012.04.004.

Torres-Freyermuth, A., Losada, I.J., Lara, J.L., 2007. Modeling of surf zone processes on a natural beach using Reynolds-Averaged Navier-Stokes equations. J. Geophys. Res.: Oceans 112 (9), C09014. http://dx.doi.org/10.1029/2006JC004050.

Tsuruta, N., Khayyer, A., Gotoh, H., Suzuki, K., 2021. Development of Wavy Interface model for wave generation by the projection-based particle methods. Coast. Eng. 165, 17. http://dx.doi.org/10.1016/j.coastaleng.2021.103861.

Vacondio, R., Altomare, C., De Leffe, M., Hu, X., Le Touzé, D., Lind, S., Marongiu, J.C., Marrone, S., Rogers, B.D., Souto-Iglesias, A., 2021. Grand challenges for smoothed particle hydrodynamics numerical schemes. Comput. Part. Mech. 8 (3), 575–588. http://dx.doi.org/10.1007/s40571-020-00354-1.

van der A, D.A., Scandura, P., O'Donoghue, T., 2018. Turbulence statistics in smooth wall oscillatory boundary layer fow. J. Fluid Mech. 849, 192–230. http://dx.doi.org/10.1017/jfm.2018.403.

van der A, D.A., van der Zanden, J., O'Donoghue, T., Hurther, D., Cáceres, I., McLelland, S.J., Ribberink, J.S., 2017. Large-scale laboratory study of breaking wave hydrodynamics over a fixed bar. J. Geophys. Res.: Oceans 122, 3287–3310. http://dx.doi.org/10.1002/2016jc012072.

van der Zanden, J., van der A, D.A., Cáceres, I., Larsen, B.E., Fromant, G., Petrotta, C., Scandura, P., Li, M., 2019. Spatial and temporal distributions of turbulence under bichromatic breaking waves. Coast. Eng. 146, 65–80. http://dx.doi.org/10.1016/j.coastaleng.2019.01.006.

van der Zanden, J., van der A., D., Eltard-Larsen, B., Sospedra, J., Cáceres, I., 2018. Hydrodynamic and Turbulence Under Breaking Waves (HYBRID) Project. Technical Report, http://dx.doi.org/10.5281/zenodo.1404708.

van der Zanden, J., van der A, D.A., Hurther, D., Cáceres, I., O'Donoghue, T., Ribberink, J.S., 2016. Near-bed hydrodynamics and turbulence below a full-scale plunging breaking wave over a mobile barred bed profile. J. Geophys. Res.: Oceans 121, 6482–6506. http://dx.doi.org/10.1002/2016JC011909.

Van Rijn, L., Grasmeijer, B., Ruessink, B., 2000. Measurement Errors of Instruments for Velocity, Wave Height, Sand Concentration and Bed Levels in Field Conditions. Technical Report, Delft Hydraulics.

van Thiel de Vries, J.S.M., van Gent, M.R.A., Walstra, D.J.R., Reniers, A.J.H.M., 2008. Analysis of dune erosion processes in large-scale flume experiments. Coast. Eng. 55 (12), 1028–1040. http://dx.doi.org/10.1016/j.coastaleng.2008.04.004.

Verbrugghe, T., Domínguez, J.M., Altomare, C., Tafuni, A., Vacondio, R., Troch, P., Kortenhaus, A., 2019. Non-linear wave generation and absorption using open boundaries within DualSPHysics. Comput. Phys. Comm. 240, 46–59. http://dx.doi.org/10.1016/j.cpc.2019.02.003.

Viccione, G., Izzo, C., 2022. Three-dimensional CFD modelling of urban flood forces on buildings: A case study. J. Phys. Conf. Ser. 2162 (1), 012020. http://dx.doi.org/10.1088/1742-6596/2162/1/012020.

Wei, Z., Dalrymple, R.A., Xu, M., Garnier, R., Derakhti, M., 2017. Short-crested waves in the surf zone. J. Geophys. Res.: Oceans 122, 4143–4162. http://dx.doi.org/10.1002/2016JC012485.

Wei, Z., Li, C., Dalrymple, R.A., Derakhti, M., Katz, J., 2018. Chaos in breaking waves. Coast. Eng. 140, 272–291. http://dx.doi.org/10.1016/j.coastaleng.2018.08.001.

Wendland, H., 1995. Piecewise polynomial, positive definite and compactly supported radial functions of minimal degree. Adv. Comput. Math. 4, 389–396. http://dx.doi.org/10.1007/BF02123482.

Wienke, J., Oumeraci, H., 2005. Breaking wave impact force on a vertical and inclined slender pile-theoretical and large-scale model investigations. Coast. Eng. 52 (5), 435–462. http://dx.doi.org/10.1016/j.coastaleng.2004.12.008.

Wilczek, M., Narita, Y., 2012. Wave-number-frequency spectrum for turbulence from a random sweeping hypothesis with mean flow. Phys. Rev. E 86, 066308. http://dx.doi.org/10.1103/PhysRevE.86.066308.

Zago, V., Schulze, L., Bilotta, G., Almashan, N., Dalrymple, R., 2021. Overcoming excessive numerical dissipation in SPH modeling of water waves. Coast. Eng. 170, 14. http://dx.doi.org/10.1016/j.coastaleng.2021.104018.

Zhang, F., Crespo, A., Altomare, C., Domínguez, J., Marzeddu, A., Shang, S.P., Gómez-Gesteira, M., 2018. DualSPHysics: A numerical tool to simulate real breakwaters. J. Hydrodyn. 30, 95–105. http://dx.doi.org/10.1007/s42241-018-0010-0.

Zhou, Z., Hsu, T.J., Cox, D., Liu, X., 2017. Large-eddy simulation of wave-breaking induced turbulent coherent structures and suspended sediment transport on a barred beach. J. Geophys. Res. Oceans 122 (1), 207–235. http://dx.doi.org/10.1002/2016JC011884.